
Redefining Neural Operators in $d + 1$ Dimensions for Embedding Evolution

Haoze Song¹ Zhihao Li¹ Xiaobo Zhang² Zecheng Gan^{1,3} Zhilu Lai^{1,3} Wei Wang^{1,3}

Abstract

Neural Operators (NOs) have emerged as powerful tools for learning mappings between function spaces. Among them, the kernel integral operator has been widely used in universally approximating architectures. Following the original formulation, most advancements focus on designing better parameterizations for the kernel over the original physical domain (with d spatial dimensions, $d \in 1, 2, 3, \dots$). In contrast, embedding evolution remains largely unexplored, which often drives models toward brute-force embedding lengthening to improve approximation, but at the cost of substantially increased computation.

In this paper, we introduce an auxiliary dimension that explicitly models embedding evolution in operator form, thereby redefining the NO framework in $d + 1$ dimensions (the original d dimensions plus one auxiliary dimension). Under this formulation, we develop a Schrödingerised Kernel Neural Operator (SKNO), which leverages Fourier-based operators to model the $d + 1$ dimensional evolution. Across more than ten increasingly challenging benchmarks, ranging from the 1D heat equation to the highly nonlinear 3D Rayleigh–Taylor instability, SKNO consistently outperforms other baselines. We further validate its resolution invariance under mixed-resolution training and super-resolution inference, and evaluate zero-shot generalization to unseen temporal regimes. In addition, we present a broader set of design choices for the lifting and recovery operators, demonstrating their impact on SKNO’s predictive performance.

1. Introduction

Neural Operators (NOs) (Li et al., 2021; Kissas et al., 2022; Kovachki et al., 2023; Wu et al., 2023; Li et al., 2023a; Rahman et al., 2023; Wu et al., 2024b) parameterize mappings between two function spaces. Specifically, given inputs, they output function values corresponding with adaptable query coordinates in the continuous domain (with d dimensions, $d = 1, 2, 3, \dots$) where functions are originally defined. For operators mapping input to certain output functions defined on a d dimensional domain, there are corresponding d dimensional PDEs describing the governing law between variables of the target system. Once the in/output functions are chosen, the solution operator depends on the governing PDE type. A main challenge for representing different operators is that the corresponding d dimensional PDE types vary across different systems.

Traditional numerical methods (Bangerth, 2008; Abdulle, 2009) tackle this by explicitly converting d dimensional governing PDEs into matrices using techniques like finite element methods and finite difference methods. However, such discretized signal evolving schemes are computationally prohibitive when improving the solution accuracy on a finer grid size (Larson & Bengzon, 2013). Unlike traditional methods relying on target system PDEs, common neural networks (NNs) universally learn the mapping between discretized input/output signal pairs on a grid in the d dimensional domain (Hornik et al., 1989; Lagaris et al., 1998), offering efficiency and adaptability to various governing PDE types. However, their predicted solution is limited by the grid size of signals (Obiols-Sales et al., 2020; Khoo et al., 2021), suffering from similar problems as numerical methods, i.e., the trade-off between computational costs (training speed, memory allocation, etc.) and accurate predictions on finer grids.

Since the problem for common neural networks lies in the size of signal grids, neural operators come: learning operators rather than just matrices, because PDEs with certain conditions evolve continuous functions rather than discretized signals. A natural extension from matrix to operator is to define a kernel integration to operate on d dimensional functions fitted to the original signals, which has been widely used in modeling neural operators (Li et al., 2021; Liu-Schiaffini et al., 2024; Wu et al., 2024a; Li et al., 2020b).

¹The Hong Kong University of Science and Technology (Guangzhou), Guangzhou, China ²Southwest Jiaotong University, Chengdu, China ³The Hong Kong University of Science and Technology, Hong Kong, China. Correspondence to: Haoze Song <hsong492@connect.hkust-gz.edu.cn>.

As a new paradigm for solving PDEs, prior studies (Li et al., 2020a; 2025) have reported that such NOs can achieve errors that are at least an order of magnitude smaller than the common NN.

Specifically, these neural operators empirically introduce a function whose value is an embedding vector, and evolve it by d dimensional kernel integral operators. Keeping activations the same, recent advancements have developed effective modules, such as graph aggregation (Li et al., 2020a;b; 2025), spectral convolution (Li et al., 2021; Wen et al., 2022), and attention mechanism (Wu et al., 2024a; Xiao et al., 2024), to better approximate the linear kernel integral operators defined on the d dimensional domain. However, they have little discussion on modeling the evolution of embeddings from input/output functions: Like the common NN, they utilize matrix multiplication directly on embeddings to evolve them in an Euclidean space by default.

For example, advanced methods (Li et al., 2023b; Wu et al., 2024a; Li et al., 2025), especially transformer-based architectures, often increase the embedding size to better capture embedding evolution, but this incurs a substantial quadratic computational cost. A common compromise is to use multi-heads that effectively form a larger block-diagonal interaction (head-wise mixing) rather than a dense, fully coupled matrix, which would more faithfully capture global dependencies during embedding evolution. However, this head-wise factorization restricts cross-head communication, so global coupling must be recovered indirectly through depth and repeated mixing, further increasing compute.

In summary, current NOs still rely on discretized matrices to model how embeddings evolve. Analogous to the previous success on operator learning, can we utilize operator designs on embeddings to reduce the computational overhead of brute-force embedding lengthening, while preserving (or even improving) approximation quality?

To address this, we depart from the conventional formulation that evolves d dimensional embedding functions over the physical domain. Instead, we explicitly model the evolution as happening simultaneously in (i) the d dimensional physical domain; and (ii) an additional axis representing embedding evolution. Concretely, we introduce an auxiliary dimension and lift the embedding function to a $(d + 1)$ dimensional domain, which is inspired by the Schrödingerisation method in quantum simulation of PDEs (Jin et al., 2024). A detailed demonstration is provided in Sec. 2.1.

After clarifying the $d+1$ dimensional evolving pipe of neural operators, we correspondingly redefine neural operators in the $d + 1$ dimensional domain (i.e., original d dimensions plus one auxiliary dimension). Following this framework, we implement the Schrödingerised Kernel Neural Operator (SKNO) by combining Fourier-based kernel modules in the

original domain and along the auxiliary dimension. Our main contributions in this work are summarized as follows:

- We redefine the current NO framework where embedding functions are defined on a new $d + 1$ dimensional domain, providing a new perspective to model the embedding evolution in neural operators, see Sec.2.
- We design our Schrödingerised Kernel Neural Operator (SKNO) within the $d + 1$ dimensional NO framework with Fourier-based blocks, utilizing $d + 1$ dimensional kernel integral operators with the aid of residuals, see Sec.3.
- We demonstrate the state-of-the-art performance of our SKNO with the $(d + 1)$ -dimensional kernel integration implementation across a diverse set of more than ten benchmarks with varying levels of approximation difficulty. In addition, we conduct model-specific studies, including mixed-training, super-resolution, zero-shot generalization to unseen temporal regimes, and ablation experiments, and further explore the impact of different lifting and recovering operator choices we provide.

2. Neural Operator in $d + 1$ Dimensions

2.1. Demonstrations of $d + 1$ Dimensional Evolution

To clarify the $d + 1$ dimensional evolving mechanism in Sec.1, we demonstrate how the d dimensional linear PDEs are transformed into their $d + 1$ dimensional versions after introducing an auxiliary dimension p :

Example 1 (Heat Equation (Jin et al., 2022; 2023)). *Consider the initial-value problem of the heat equation:*

$$\partial_t u = \partial_{xx} u, \quad (d \text{ dimensional heat equation}) \quad (1)$$

$$u(x, t = 0) = u_0, \quad (d \text{ dimensional input}) \quad (2)$$

where $u = u(x, t)$, $x = (x_1, x_2, \dots, x_d) \in \mathbb{R}^d$, $t \geq 0$. Let $d = 1$, which can be easily generalized to arbitrary d . Our goal is to construct a $d + 1$ dimensional pipe that evolves the initial condition $u_0 = u(x, t = 0)$ to the solution $u_1 = u(x, t = 1)$, shown in Fig.1 A.

Step 1: Warped Phase Transformation. Define a transformation from $u(x, t)$ to $v(x, p, t)$ by introducing an auxiliary dimension $p \in (-\infty, \infty)$:

$$v(x, p, t = 0) = v_0(x, p) = e^{-|p|} u_0. \quad (3)$$

Step 2: $d + 1$ Dimensional Phase-space Heat Equation. Combine Equ.1, 2 and 3, obtain:

$$\partial_t v(x, p, t) = -\partial_p \partial_{xx} v(x, p, t). \quad (4)$$

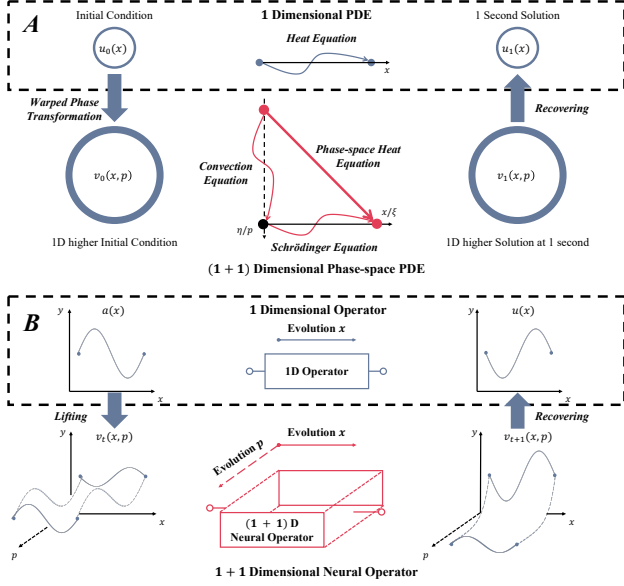


Figure 1. A-Schrödingerisation: Classical linear PDEs can be transformed into their $d + 1$ dimensional version (here $d = 1$ for visualization) by a warped phase transformation, e.g., heat equation \rightarrow phase-space heat equation. And it can be represented by a group of Schrödinger / convection equations after taking the Fourier Transform on p / x . **B-Neural Operator:** Different d dimensional linear operators can be similarly lifted to their $d + 1$ versions, and parameterized by the $d + 1$ dimensional Neural Operator which flexibly represents the evolution on both x and p .

Step 3: Recovering to d Dimensional Solution. After evolving $v_0 \mapsto v_1 := v(x, p, t = 1)$ by Equ.4, Recover u_1 by integrating along p :

$$u_1(x) = \int_{-\infty}^{\infty} \chi(p)v_1(x, p)dp, \quad (5)$$

where $\chi(p)$ has multiple choices and depends on the introduced transformation form in Step 1. Here $\chi(p)$ can be formed as the step function or delta function.

For Equ.3, if taking fourier transform on p ($\mathcal{F}_p : p \rightarrow \eta$), one gets a group of uncoupled Schrödinger equations (operators), over all η ; If taking fourier transform on x ($\mathcal{F}_x : x \rightarrow \xi$), one gets a group of uncoupled convection equations (operators), over all ξ . Generally for $v(t)$, discrete signals on x and p from $v(x, p, t)$, one gets a Hamiltonian system by taking the discrete fourier transform (DFT) on p . For Equ.3, the Hamiltonian system can be represented by further taking DFT on x :

$$\frac{d}{dt} \hat{v}(t) = i(D_\mu^2 \otimes D_\mu) \hat{v}(t), \quad (6)$$

where $\hat{v}(t)$ is derived after taking DFT for $v(t)$ on p and x , and the same notation $D_\mu = \text{diag}(\mu_{-N_p/2}, \dots, \mu_{N_p/2})$, which denotes a diagonal matrix with N_p grid points in

one dimension, is employed since little confusion will arise. Here, the diagonal coefficient complex matrix $i(D_\mu^2 \otimes D_\mu)$ is from taking DFTs on the x and p domain for $-\partial_p \partial_{xx}$ in Equ.3.

Example 2 (Advection Equation and Other Linear PDEs). Similar process and result on advection equation as Example 1 with introducing corresponding warped phase transformation $v_0 = \sin(p)u_0$, $p \in [-\pi, \pi]$. Limited by pages, for more discussion of other PDE types, refer to (Jin et al., 2023).

According to (Jin et al., 2023; Jin & Liu, 2024), the warped phase functions and the recovery weight functions along p are chosen based on systems governed by different linear PDEs. Generally, we introduce the auxiliary dimension p with a parameterized setting: explicitly redefining the neural operator embedding functions and their evolution in a $d + 1$ dimensional formulation below, as illustrated in Fig. 1 B.

2.2. Operator Learning in $d + 1$ Dimensions

Problem Setup Denote that $D_x \subset \mathbb{R}^d$ is a bounded, open set with d dimensions. Given functions $a(x) \in \mathcal{A}(D_x; \mathbb{R}^{d_a})$ and $u(x) \in \mathcal{U}(D_x; \mathbb{R}^{d_u})$ with $x = (x_1, x_2, \dots, x_d) \in D_x$, our goal is to approximate mapping operators $\mathcal{G}: a \mapsto u := \mathcal{G}[a]$. Here \mathcal{A} and \mathcal{U} are (suitable subsets of) Banach spaces, where functions a and u take values in \mathbb{R}^{d_a} and \mathbb{R}^{d_u} ($d_a, d_u \in \mathbb{N}$), respectively.

Similar to Example 1, we split our framework into three main components based on (Li et al., 2021) for redefining the $d + 1$ dimensional neural operator framework:

Lifting We prepare the $d + 1$ dimensional function $v(x, p) \in \mathcal{V}(D; \mathbb{R})$ for system evolving in $d + 1$ dimensions, where $D = D_x \times D_p$. Given that we only have the input signal on the original domain, we design the lifting operator \mathcal{P} with a separated form as Equ.3, which involves multiplying a learnable function $w(p)$, $p \in D_p$, $w \in \mathbb{R}^{d_a}$ whose values can be optimized by the back-propagation algorithm in neural implementations. The mathematical description of lifting operator \mathcal{P} is:

$$v(x, p) = \mathcal{P}[a](x, p) = w^T(p)a(x). \quad (7)$$

$d + 1$ Dimensional Evolution We define the kernel integral operator on the $d + 1$ dimensional domain by introducing an auxiliary variable p . Specifically, given a kernel $\kappa: \mathbb{R}^{2(d+1)} \rightarrow \mathbb{R}$, we define:

$$\mathcal{K}[v](x, p) = \iint_{D_x \times D_p} \kappa(x, y, p, p')v(y, p')dydp'. \quad (8)$$

To assemble a neural operator capable of approximating non-linear operators, we model the (non-linear) evolution using a

standard and well-established structure: iterative stacking of linear operators \mathcal{L} and nonlinear activations σ , as shown in Fig. 2. When the linear block admits a well-defined operator parameterization, the overall nonlinear approximation can be justified via universal approximation theory (Kovachki et al., 2021). Note that, the concrete implementation of \mathcal{L} , whose core component is \mathcal{K} in Eq. 8, depends on the specific model design; see Sec. 3.1.

Recovering After evolving $v(x, p)$, we take weighted integration on D_p with a learnable function $\chi(p)$, $\chi \in \mathbb{R}^{d_u}$ to recover solution $u(x)$ back to the original domain. Define Recovering Operator \mathcal{Q} :

$$u(x) = \mathcal{Q}[v](x) = \int_{D_p} \chi(p)v(x, p)dp. \quad (9)$$

Given all the definitions introduced above, now we assemble our neural operator framework to approximate \mathcal{G} in the problem setup as follows:

$$\begin{aligned} \mathcal{G}[a] &= (\mathcal{Q} \circ \mathcal{M} \circ \mathcal{P})[a] \\ &\approx (\mathcal{Q} \circ (\sigma_{L-1} \circ \mathcal{L}_{L-1}) \circ \dots \circ (\sigma_0 \circ \mathcal{L}_0) \circ \mathcal{P})[a], \end{aligned} \quad (10)$$

where $v_{l+1} = (\sigma_l \circ \mathcal{L}_l)[v_l]$, $l = 0, 1, \dots, L - 1$. Here, each \mathcal{L}_l denotes a general learnable $d + 1$ dimensional linear operator, and σ_l can be a non-linear activation function or a shallow MLP as a non-linear operator (p -dim-evolving operator + activation + p -dim-evolving operator).

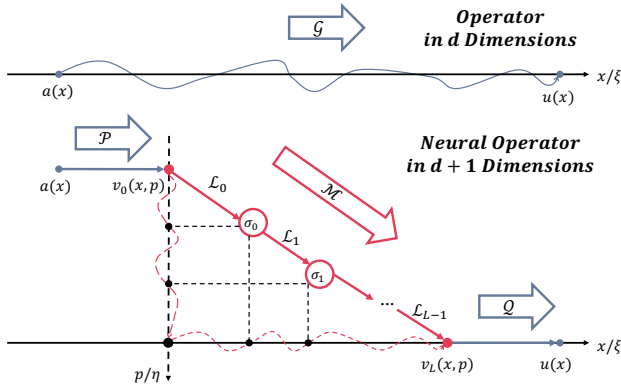


Figure 2. Neural Operator framework in $d + 1$ dimensions clarification. *Above*: Target d dimensional operator \mathcal{G} , mapping input $a(x)$ to output $u(x)$; *Below*: Neural Operator $d + 1$ dimensional framework, where the lifted $d + 1$ dimensional function $v(x, p)$ from input $a(x)$ evolves iteratively through linear and non-linear updates and finally recover to d dimensional solution $u(x)$.

3. Schrödingerised Kernel Neural Operator

In this section, we show implementation details of our proposed **Schrödingerised Kernel Neural Operator (SKNO)**

within the redefined $d + 1$ dimensional framework, which is informed by the Schrödingerisation process in Sec.2. Sec.3.1 introduces the architecture and implementation of the SKNO. Different from Sec.3.1 which mainly follows the evolving in D_x , Sec.3.2 focuses on how SKNO captures the evolution along the auxiliary dimension.

3.1. Model Architecture and Implementation

An overview of the SKNO architecture is shown in Fig. 3. Except for the lifting and measuring modules, we implement the SKNO by constructing signal propagators with the kernel integration in Equ.8, and with the aid of residuals. Each of them propagates the $d + 1$ dimensional signal v_l with different structural biases on global or local regions on D_x .

Lifting and Recovering For the lifting module in SKNO, we choose the simplest way to implement $w(p)$ in Equ.7 with a linear layer, which balances the representation flexibility with computational efficiency. From Example 1, Step 3, we have flexible implementation choices for $\chi(p)$ in Equ.9. For highlighting the power of our $d + 1$ dimensional evolving design, here we keep using MLP as the projection layer in other works, where the last linear layer implements the integration in Equ.9 as numerical quadrature. We also conducted comprehensive experiments and further explanations of different implementation choices for \mathcal{P} and \mathcal{Q} in Sec.4.2.

$d + 1$ Dimensional Signal Propagation on D_x As illustrated in Fig.3, we employ $(L - 1)$ global propagators and one last local propagator for modeling the underlying $d + 1$ dimensional function evolution in D_x .

Spectral Convolution Operator In the Schrödingerisation process (Jin et al., 2023) like Example 1 and 2, different differential operators with respect to x (e.g. $\partial_x, \partial_{xx}, \dots$) can be represented by a complex diagonal matrix in Fourier domain of x according to the properties of Fourier Transform.

Based on that, we leverage the implementation of spectral convolution operator in (Li et al., 2021), which uses a learnable complex vector equivalent to a diagonal matrix in the Fourier domain of D_x , to parameterize the evolving operator related to $d + 1$ dimensional PDEs. A typical example is shown in 6. In practice, the complex vector is truncated for working on different grid sizes:

$$\text{SpectralConvOp}(v_l) = F_x^{-1}(\text{trun_diag}(F_x(v_l))), \quad (11)$$

where F_x and F_x^{-1} denote DFT and Inverse DFT (accelerated by Fast Fourier Transform (FFT) in practice). The `trun_diag()` represents the element-wise multiplication between a learnable truncated complex vector and signal slices of v_l on the transformed grid ξ .

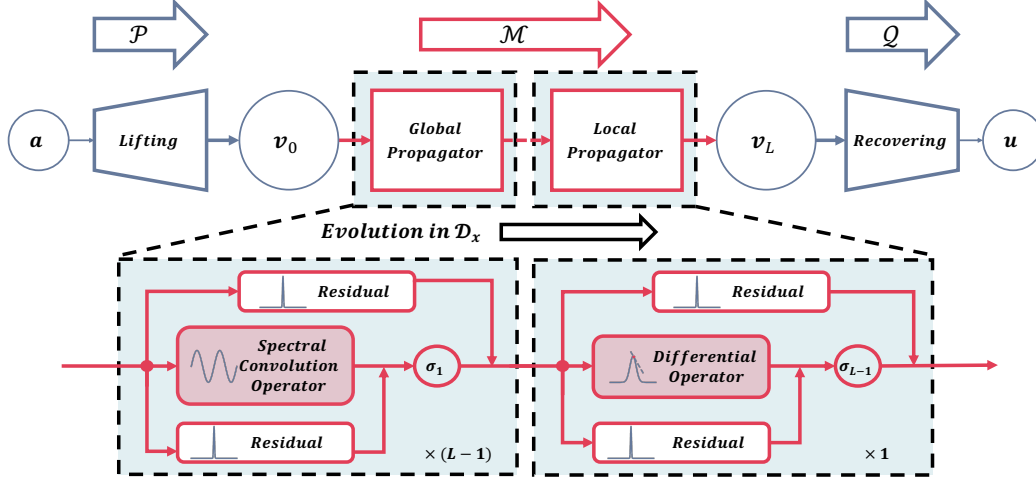


Figure 3. Overview of the Schrödingerised Kernel Neural Operator (SKNO) architecture. The input signal \mathbf{a} is lifted to a $d + 1$ dimensional signal \mathbf{v}_0 through the preparation lifting module. Such a $d + 1$ dimensional signal evolves through $(L - 1)$ global propagators and one local propagator in \mathcal{D}_x , capturing both global and local signal changes. The measuring module recovers the output signal \mathbf{u} from evolved \mathbf{v}_L .

Differential Operator Since the truncation in Sec.3.1 prefers to propagate signals in a relatively global scope, we compensate for possible local information lost by propagating the finite difference derivative of x on the local region. Details are provided in Appendix B.

Linear Block with Residuals With above two implementations of $d + 1$ dimensional kernel integral operators in Equ.8, we specified the linear block \mathcal{L} in Equ.10 with two parts: kernel integral operator \mathcal{K}_l and residual operator $\bar{\mathcal{W}}_l$:

$$\mathcal{L}_l[v_l](x, p) = (\mathcal{K}_l + \bar{\mathcal{W}}_l)[v_l](x, p), \quad (12)$$

where $\bar{\mathcal{W}}_l[v_l](x, p) = (\mathcal{I} + \mathcal{W}_l)[v_l](x, p) = v_l(x, p) + \int_{\mathcal{D}_p} w_l(p, p')v_l(x, p')dp'$. Here, \mathcal{W}_l is implemented by a shallow MLP and \mathcal{I} is implemented by a residual connection.

3.2. Evolution along the Auxiliary Dimension

In this section, we will show our model captures the evolution along the extra dimension with general linear PDEs:

$$\frac{\partial v_t(x_i, p)}{\partial t} = \left(\sum_{k=1}^K a_k(p) \frac{\partial^k}{\partial p^k} + b(p) \right) v_t(x_i, p) \quad (13)$$

where $x_i = (x_{i_1}, \dots, x_{i_d})$, $i = (i_1, \dots, i_d)$. Note that the same conclusion also works for ξ_i . And K represents the highest order of the differential operator with respect to p .

After discretizing time t across deep layers (Chen et al., 2018), Equ. 13 is implemented using a forward finite-difference (Euler) update. The step size is set to $\Delta t = 1$ for notational simplicity, and can be treated as learnable or

tuned in practice.

$$v_{l+1}(x_i, p) - v_l(x_i, p) = (\mathcal{K}_l + \mathcal{W}_l)[v_l](x_i, p), \quad (14)$$

which is exactly our linear block in Equ. 12. For discrete signals along p , we implement the right-hand side of Equ. 14 as $F_p^{-1} \tilde{A} F_p + \mathbf{b}$, where \tilde{A} denotes a learnable matrix in the Fourier domain over p , and \mathbf{b} corresponds to the discretized $b(p)$. As illustrated in Fig. 4, while other methods vary the discretization resolution of (p) to capture the evolving dynamics in Equ. 13, our model explicitly incorporates both the weighted differential operator represented in the Fourier domain over p (SKNO, right) and the bias term (SKNO, left), thereby aligning with the general linear PDE form in Equ. 13. Extended implementations along p are provided in Appendix B.

By iteratively updating the $d+1$ dimensional signal using the combination of the operator designs in Sec.3.1 and Sec.3.2, our SKNO model aligns itself well with $d + 1$ dimensional PDEs, which effectively offers improved scalability and adaptability over previous methods.

4. Experiments

4.1. General Setting

Benchmarks We evaluate the proposed model on more than ten diverse benchmarks spanning a wide spectrum of PDE dynamics. To highlight the effectiveness of our evolving kernel integral design, we first compare different kernel parameterizations on the PDE operators introduced in Sec. 2.1, including the 1D heat equation (Shin et al., 2022) and the 1D advection equation (Takamoto et al., 2022). We then evaluate full models on a broader set of

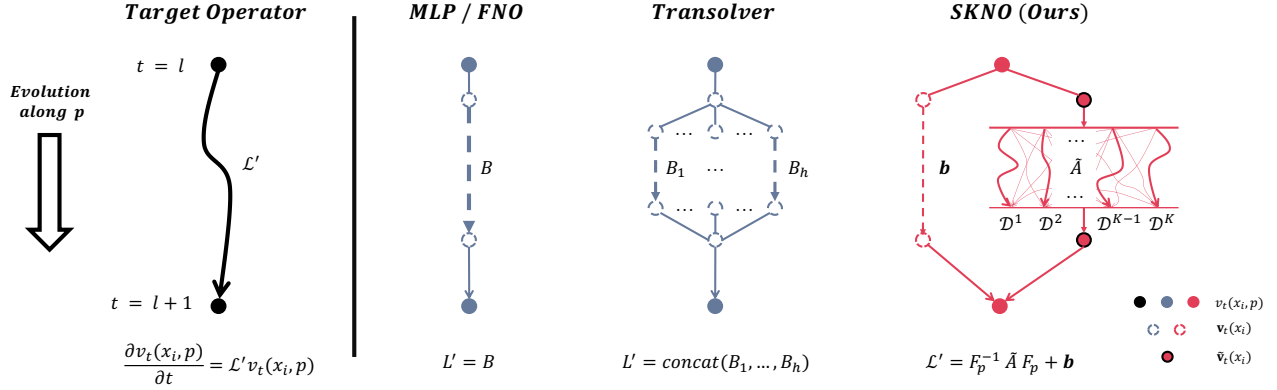


Figure 4. Evolution along the auxiliary dimension and corresponding neural operator implementations. *Left*: The target operator \mathcal{L}' governs the evolution along p . *Right*: Whereas prior methods rely on discretized matrices at each p location, our model captures this evolution using operator modules acting on dual spaces.

PDE systems, conducting extensive experiments on the 1D Burgers equation; 2D Darcy flow with discontinuous coefficients; 2D incompressible Navier–Stokes at low viscosity ($1e-5$) (Li et al., 2021; Wu et al., 2024a); 2D Gray–Scott Reaction–Diffusion (Kassai Koupai et al., 2024); and the highly unstable 3D Rayleigh–Taylor Instability (Ohana et al., 2024). Additional benchmarks and detailed results are provided in Appendix B.

Baselines and Configurations We compare our model with various d dimensional neural implementations, including DeepONet (Lu et al., 2021), Fourier Neural Operator (FNO) (Li et al., 2021), Convolutional Neural Operator (CNO) (Raonic et al., 2023a), and transformer-based model Transolver (Wu et al., 2024a). All models are trained under their officially recommended optimal configurations, following the settings reported in their respective papers and official codes. For benchmarks such as 1D Burgers, 2D Darcy Flow, and 2D Gray–Scott, we train each model for 500 epochs with no physical prior regularization, using only relative L_2 loss. For the incompressible 2D Navier–Stokes, we ensure fairness by matching comparable training time scales, accounting for differences in training speed between transformer-based and other operator architectures. All experiments are run on a single *Nvidia GeForce RTX 4090* GPU. Complete configurations are provided in Tab.7.

4.2. Main Results and Analysis

Results SKNO consistently outperforms existing methods, achieving the lowest relative L_2 error with competitive training cost. Tab. 1 summarizes the performance of different \mathcal{L} parameterizations across representative models: the Fourier integral operator in FNO, the physics-attention block in Transolver, and SKNO’s spectral convolution operator acting on $d + 1$ dimensional functions. All modules are evaluated with their original lifting and recovering com-

Table 1. Different \mathcal{L} parameterizations’ performance on learning operators governed by 1D Heat and Advection Equations.

Linear Blocks	Error
1D Heat Equation	
FNO (1 mode, 4 grid p)	9.305e-1
Transolver (1 slice, 4 grid $p / 2$ heads)	9.060e-1
Transolver (4 slices, 4 grid $p / 2$ heads)	8.988e-1
Transolver (4 slices, 4 grid $p / 1$ head)	8.987e-1
Ours (1 mode, 4 grid p)	2.637e-3
1D Advection Equation	
Transolver (8 slices, 16 grid $p / 4$ heads)	7.118e-1
Transolver (8 slices, 16 grid $p / 2$ heads)	6.984e-1
Transolver (8 slices, 16 grid $p / 1$ head)	6.828e-1
FNO (8 modes, 16 grid p)	6.012e-2
Ours (8 modes, 16 grid p)	1.979e-2

ponents and without additional positional encoding (see Appendix B).

For the heat equation experiment, the solution at $t = 1$ is predicted following Example 1, using the same truncation settings as in practice (i.e., truncated modes or slices, both of which parameterize an invertible aggregation on D_x). For the advection equation, these kernels are tested in an autoregressive setting to validate performance on sequential prediction with concatenated input quantities. Specifically, the reported error corresponds to predicting the next 10 time steps autoregressively given the previous 10.

While other modules are constrained by their evolution design along p , SKNO removes this bottleneck and stably captures the $d + 1$ dimensional evolution. Across the benchmarks in Tab. 2, Tab. 13, and Tab. 15, SKNO achieves

Table 2. Main experimental results for the 1D Burgers, 2D Gray-Scott (GS), 2D incompressible NS and 3D Rayleigh-Taylor Instability. For 2D GS and NS, errors are measured within the next 10 time steps with autoregressive predictions.

Benchmark	1D Burgers Equation				2D Gray-Scott			
	DeepONet	FNO	Transolver	SKNO	DeepONet	FNO	Transolver	SKNO
Training Time	2.07 min	6.86 min	94.23 min	15.51 min	3.01 min	9.64 min	234.96 min	20.11 min
Rel. L_2 Error	8.991e-2	6.479e-4	6.277e-3	5.475e-4	1.528e-1	2.425e-2	3.573e-2	1.298e-2
	2D Incompressible NS				3D Rayleigh-Taylor Instability			
	DeepONet	FNO	Transolver	SKNO	DeepONet	FNO	Transolver	SKNO
Training Time	865.75 min	773.33 min	1263.33 min	708.93 min	1.56 min	5.12 min	135.03 min	10.31 min
Rel. L_2 Error	3.448e-1	1.280e-1	1.002e-1	8.717e-2	5.731e-2	5.219e-2	5.723e-2	4.471e-2

state-of-the-art (SOTA) performance, with training time comparable to FNO, which is widely recognized for balancing speed and accuracy. Visualizations in Fig. 9 and Fig. 10 further demonstrate that SKNO excels in capturing sharp, local details, such as discontinuities at material interfaces and vorticity in low-viscosity fluid flows. For complete experimental settings, case studies, and complete results, see Appendix B.

Resolution Invariance A key advantage of neural operators is their resolution invariance. To verify this, we design novel experiments where training data of mixed resolutions are combined. Tab. 13 shows that SKNO consistently achieves the best accuracy, even under randomly mixed training resolutions, demonstrating robustness. In addition, we further evaluate super-resolution performance on the 1D Burgers equation, 2D Darcy flow, and the challenging ERA5 wind field prediction task. All models are trained on a fixed resolution and tested on lower and higher ones. As shown in Fig. 5, SKNO maintains a consistently low relative L_2 error across resolutions, significantly outperforming FNO on 1D Burgers. Other results in Tab. 12 and Tab. 14 indicate that competing models exhibit large error fluctuations when resolution increases, revealing their instability in generalizing across resolutions. In contrast, SKNO provides more stable and reliable predictions across varying scales.

Different Lifting and Recovering Operators We explore a broader set of lifting and recovering operators we have discussed to test their impact on the output solution. Specifically, we fix \mathcal{P} with a linear layer and vary the integration weights $\chi(p)$ for \mathcal{Q} . Tab. 4 shows that all recovering designs proposed in Example 1 perform well on the heat equation, where the Mean and Linear can also be properly scaled since the symmetry of $w(p)$. Amazingly, some predefined recovering operators can still work on complex Darcy cases, where the complete evolution provides detailed local changes reflecting on D_x , see Fig. 8. Combining results from Tab. 4 and Tab. 5 on 2D Darcy, we find that for functions with complex topology on D_x , a continuous non-linear trans-

Table 3. Ablation study for SKNO on 2D Darcy. The Linear Residual is $\tilde{\mathcal{W}}_l$ in Linear Block \mathcal{L} , while the non-linear one is out of \mathcal{L} .

Configuration	Error
w.o. Double Res.	1.363e-2
w.o. Linear Res.	8.284e-3
w.o. Non-linear Res.	7.621e-3
w.o. \tilde{A} along p dim	8.804e-3
w.o. b along p dim	6.827e-3
w.o. Global Propagators	1.584e-1
w.o. Local Propagator	5.715e-3
Baseline (SKNO)	5.555e-3

formation on $d + 1$ dimensional signals, either after first lifting or before last recovering, can help it adjust the $d + 1$ dimensional propagating structure. The best performance with MLP-Linear combination is consistent with the MLP-Linear implementation in Transolver (Wu et al., 2024a) for handling complex topology.

Ablation We conduct a detailed ablation study on 2D Darcy (Tab. 3) to evaluate the contribution of different components. Removing both linear and non-linear residual layers causes a significant performance degradation, confirming their necessity for modeling complex $d + 1$ dimensional evolution. Similarly, omitting the p differential operator in the Fourier domain \tilde{A} or the bias term b from the auxiliary dimension dynamics results in higher errors, where the introduced \tilde{A} contributes more to the model prediction. Finally, we separate the contributions of the global and local propagators. The global propagator captures long-range dependencies, while the local propagator refines predictions in regions with sharp transitions, corresponding to the scale of rebounded errors after masking one of them and keeping another.

Table 4. The error on 1D Heat and 2D Darcy with different Q implementations.

Q	Delta	Step	Mean	Linear	MLP	MLP (Dropout)
1D Heat Equation						
Error	2.538e-3	2.538e-3	2.538e-3	2.538e-3	<u>2.637e-3</u>	7.928e-3
2D Darcy Flow						
Error	5.752e-3	1.402e-2	5.717e-3	5.741e-3	5.555e-3	<u>5.678e-3</u>

 Table 5. The error on 2D Darcy with different P , Q combinations.

$P \backslash Q$	Linear	MLP
Constant	8.738e-3	8.791e-3
Linear	5.741e-3	5.555e-3
MLP	5.952e-3	6.614e-3
MLP (Dropout)	5.451e-3	5.845e-3

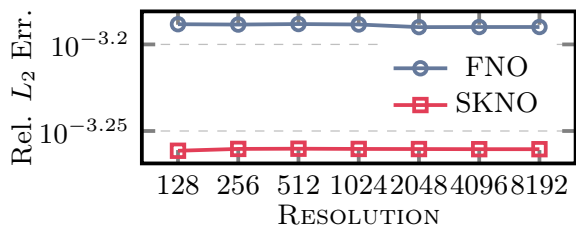


Figure 5. Model performance on the Burgers equation with grid size ranging from 128 to 8192.

Other Experiments More experiment results and visualizations can be found in the Appendix, mainly including (i) Zero-shot Generalization to Unseen Temporal Regimes: We have shown the SOTA performance of SKNO on 2D incompressible Navier-Stokes in Fig. 15. (ii) Other Operators along p : We show that other operator choices along p like physics-attention (Wu et al., 2024a) also benefit from adopting the $d + 1$ dimensional operator design, see Tab. 11.

5. Conclusion, Limitations and Future work

In this work, we redefine neural operators within a $d + 1$ dimensional framework. Building on this formulation, we propose the Schrödingerised Kernel Neural Operator (SKNO), which employs an efficient parameterization of the $d + 1$ dimensional kernel integral operator. Across more than ten benchmarks, SKNO achieves state-of-the-art accuracy with competitive computational efficiency. Moreover, its demonstrated resolution invariance, zero-shot generalization to unseen temporal regimes, and comprehensive ablation studies jointly support the robustness and validity of the proposed $d + 1$ dimensional designs. Taken together, these results not only establish $d + 1$ dimensional neural operators such as SKNO as a simple yet highly effective extension of prior neural operators, but also motivate broader exploration of operator design and learning over the full $d + 1$ problem domain.

An important open problem is to develop quantitative criteria for comparing neural operators at their optimizer-attained local minima. Because training navigates a high-dimensional error landscape over a large set of kernel pa-

rameters, both the optimization trajectory and the attained minimum can vary substantially across architectures. While existing models (e.g., (Li et al., 2021; Hao et al., 2023; Wu et al., 2024a)) and related theoretical analyses (e.g., (Kovachki et al., 2021; Lanthaler et al., 2025; Furuya et al., 2025)) provide approximation-oriented results, they offer limited insight into the properties of the minima selected by practical optimization. As future work, we will focus on comparing different aggregation designs and the associated propagation parameters across layers, and quantify how these choices affect neighborhood-averaged training and test errors around local minima.

6. Ethics and Reproducibility Statements

This work does not involve human subjects, personal data, or other sensitive information. All experiments were conducted on publicly available or synthetically generated datasets. To ensure reproducibility, we provide detailed descriptions of the experimental setup, including model architectures, training procedures, and evaluation protocols. The code and datasets used in this study will be made publicly accessible upon publication. For readers, the code implementations and related configurations are included in the supplementary materials.

References

- Abdulle, A. The finite element heterogeneous multiscale method: a computational strategy for multiscale pdes. *GAKUTO International Series Mathematical Sciences and Applications*, 31:135–184, 2009.
- Adalsteinsson, D. and Sethian, J. A. A fast level set method for propagating interfaces. *Journal of computational physics*, 118(2):269–277, 1995.
- Bangerth, W. A framework for the adaptive finite element solution of large-scale inverse problems. *SIAM Journal on Scientific Computing*, 30(6):2965–2989, 2008.
- Barron, A. R. Universal approximation bounds for superpositions of a sigmoidal function. *IEEE Transactions on Information theory*, 39(3):930–945, 2002.

- Brandstetter, J., van den Berg, R., Welling, M., and Gupta, J. K. Clifford neural layers for pde modeling. In *the 11th International Conference on Learning Representations*, 2023.
- Burark, P., Tiwari, K., Rashid, M. M., AP, P., and Krishnan, N. A. Codbench: a critical evaluation of data-driven models for continuous dynamical systems. *Digital Discovery*, 3(6):1172–1181, 2024.
- Cantwell, B. J. *Introduction to symmetry analysis*. Cambridge University Press, 2002.
- Cao, Q., Goswami, S., and Karniadakis, G. E. Laplace neural operator for solving differential equations. *Nature Machine Intelligence*, 6(6):631–640, 2024.
- Cao, S. Choose a transformer: Fourier or galerkin. In *Advances in Neural Information Processing Systems*, 2021.
- Chen, R. T., Rubanova, Y., Bettencourt, J., and Duvenaud, D. K. Neural ordinary differential equations. *Advances in Neural Information Processing Systems*, 2018.
- Chen, T. and Chen, H. Universal approximation to nonlinear operators by neural networks with arbitrary activation functions and its application to dynamical systems. *IEEE Transactions on Neural Networks*, 6(4):911–917, 1995.
- Chinesta, F., Ladeveze, P., and Cueto, E. A short review on model order reduction based on proper generalized decomposition. *Archives of Computational Methods in Engineering*, 18(4):395–404, 2011.
- Ern, A. and Guermond, J.-L. *Theory and practice of finite elements*, volume 159. Springer, 2004.
- Furuya, T., Taniguchi, K., and Okuda, S. Quantitative approximation for neural operators in nonlinear parabolic equations. In *the 13th International Conference on Learning Representations*, 2025.
- Guibas, J., Mardani, M., Li, Z., Tao, A., Anandkumar, A., and Catanzaro, B. Adaptive fourier neural operators: Efficient token mixers for transformers. In *the 10th International Conference on Learning Representations*, 2022.
- Hao, Z., Wang, Z., Su, H., Ying, C., Dong, Y., Liu, S., Cheng, Z., Song, J., and Zhu, J. Gnot: A general neural operator transformer for operator learning. In *Proceedings of the 40th International Conference on Machine Learning*, 2023.
- He, K., Zhang, X., Ren, S., and Sun, J. Deep residual learning for image recognition. In *Proceedings of the IEEE conference on computer vision and pattern recognition*, pp. 770–778, 2016.
- Hersbach, H., Bell, B., Berrisford, P., Hirahara, S., Horányi, A., Muñoz-Sabater, J., Nicolas, J., Peubey, C., Radu, R., Schepers, D., et al. The era5 global reanalysis. *Quarterly journal of the royal meteorological society*, 146(730): 1999–2049, 2020.
- Hornik, K., Stinchcombe, M., and White, H. Multilayer feedforward networks are universal approximators. *Neural Networks*, 2(5):359–366, 1989.
- Jin, S. and Liu, N. Analog quantum simulation of partial differential equations. *Quantum Science and Technology*, 9:035047, 2024.
- Jin, S. and Osher, S. A level set method for the computation of multi-valued solutions to quasi-linear hyperbolic pde’s and hamilton-jacobi equations. *Communications in Mathematical Sciences*, 1(1):575–591, 2003.
- Jin, S., Liu, N., and Yu, Y. Quantum simulation of partial differential equations via schrodingerisation: technical details. *ArXiv*, abs/2212.14703, 2022.
- Jin, S., Liu, N., and Yu, Y. Quantum simulation of partial differential equations: Applications and detailed analysis. *Physical Review A*, 108:032603, 2023.
- Jin, S., Liu, N., and Yu, Y. Quantum simulation of partial differential equations via schrödingerization. *Physical Review Letters*, 133(23):230602, 2024.
- Kassaï Koupaï, A., Mifsut Benet, J., Yin, Y., Vittaut, J.-N., and Gallinari, P. Boosting generalization in parametric pde neural solvers through adaptive conditioning. *Advances in Neural Information Processing Systems*, 2024.
- Khoo, Y., Lu, J., and Ying, L. Solving parametric pde problems with artificial neural networks. *European Journal of Applied Mathematics*, 32(3):421–435, 2021.
- Kingma, D. P. and Lei Ba, J. Adam: A method for stochastic optimization. In *the 3rd International Conference on Learning Representations*, 2015.
- Kissas, G., Seidman, J. H., Guilhoto, L. F., Preciado, V. M., Pappas, G. J., and Perdikaris, P. Learning operators with coupled attention. *Journal of Machine Learning Research*, 23(215):1–63, 2022.
- Kovachki, N., Lanthaler, S., and Mishra, S. On universal approximation and error bounds for fourier neural operators. *Journal of Machine Learning Research*, 22(290): 1–76, 2021.
- Kovachki, N., Li, Z., Liu, B., Azizzadenesheli, K., Bhattacharya, K., Stuart, A., and Anandkumar, A. Neural operator: Learning maps between function spaces with applications to pdes. *Journal of Machine Learning Research*, 24:89:1–89:97, 2023.

- Lagaris, I. E., Likas, A., and Fotiadis, D. I. Artificial neural networks for solving ordinary and partial differential equations. *IEEE Transactions on Neural Networks*, 9(5): 987–1000, 1998.
- Lanthaler, S., Li, Z., and Stuart, A. M. Nonlocality and nonlinearity implies universality in operator learning. *Constructive Approximation*, pp. 1–43, 2025.
- Larson, M. G. and Bengzon, F. *The finite element method: theory, implementation, and applications*, volume 10. Springer Science & Business Media, 2013.
- Li, Z., Kovachki, N., Azizzadenesheli, K., Liu, B., Bhattacharya, K., Stuart, A., and Anandkumar, A. Neural operator: Graph kernel network for partial differential equations. In *the 8th International Conference on Learning Representations, ICLR 2020 Workshop: Integration of Deep Neural Models and Differential Equations*, 2020a.
- Li, Z., Kovachki, N., Azizzadenesheli, K., Liu, B., Stuart, A., Bhattacharya, K., and Anandkumar, A. Multipole graph neural operator for parametric partial differential equations. In *Advances in Neural Information Processing Systems*, 2020b.
- Li, Z., Kovachki, N., Azizzadenesheli, K., Liu, B., Bhattacharya, K., Stuart, A., and Anandkumar, A. Fourier neural operator for parametric partial differential equations. In *the 9th International Conference on Learning Representations*, 2021.
- Li, Z., Huang, D. Z., Liu, B., and Anandkumar, A. Fourier neural operator with learned deformations for pdes on general geometries. *Journal of Machine Learning Research*, 24(388):1–26, 2023a.
- Li, Z., Meidani, K., and Farimani, A. B. Transformer for partial differential equations’ operator learning. *Transactions on Machine Learning Research*, 2023b.
- Li, Z., Kovachki, N., Choy, C., Li, B., Kossaifi, J., Otta, S., Nabian, M. A., Stadler, M., Hundt, C., Azizzadenesheli, K., et al. Geometry-informed neural operator for large-scale 3d pdes. *Advances in Neural Information Processing Systems*, 2024.
- Li, Z., Song, H., Xiao, D., Lai, Z., and Wang, W. Harnessing scale and physics: A multi-graph neural operator framework for pdes on arbitrary geometries. In *Proceedings of the 31st ACM SIGKDD Conference on Knowledge Discovery and Data Mining V. 1*, pp. 729–740, 2025.
- Liu-Schiaffini, M., Berner, J., Bonev, B., Kurth, T., Azizzadenesheli, K., and Anandkumar, A. Neural operators with localized integral and differential kernels. *ArXiv*, abs/2402.16845, 2024.
- Loshchilov, I. and Hutter, F. Decoupled weight decay regularization. In *the 7th International Conference on Learning Representations*, 2019.
- Lu, L., Jin, P., Pang, G., Zhang, Z., and Karniadakis, G. E. Learning nonlinear operators via deepnet based on the universal approximation theorem of operators. *Nature Machine Intelligence*, 3(3):218–229, 2021.
- Lucia, D. J., Beran, P. S., and Silva, W. A. Reduced-order modeling: new approaches for computational physics. *Progress in aerospace sciences*, 40(1-2):51–117, 2004.
- Meyer, Y. *Wavelets and operators*. Number 37. Cambridge university press, 1992.
- Obiols-Sales, O., Vishnu, A., Malaya, N., and Chandramowlishwaran, A. Cfdnet: A deep learning-based accelerator for fluid simulations. In *Proceedings of the 34th ACM International Conference on Supercomputing*, pp. 1–12, 2020.
- Ohana, R., McCabe, M., Meyer, L., Morel, R., Agocs, F., Beneitez, M., Berger, M., Burkhart, B., Dalziel, S., Fielding, D., et al. The well: a large-scale collection of diverse physics simulations for machine learning. *Advances in Neural Information Processing Systems*, 2024.
- Osher, S. and Fedkiw, R. P. Level set methods: an overview and some recent results. *Journal of Computational physics*, 169(2):463–502, 2001.
- Osher, S., Fedkiw, R., and Piechor, K. Level set methods and dynamic implicit surfaces. *Appl. Mech. Rev.*, 57(3): B15–B15, 2004.
- Qu, J., Cai, W., and Zhao, Y. Learning time-dependent pdes with a linear and nonlinear separate convolutional neural network. *Journal of Computational Physics*, 453:110928, 2022.
- Rahman, M. A., Ross, Z. E., and Azizzadenesheli, K. U-no: U-shaped neural operators. *Transactions on Machine Learning Research*, 2023.
- Raonic, B., Molinaro, R., De Ryck, T., Rohner, T., Bartolucci, F., Alaifari, R., Mishra, S., and de Bézenac, E. Convolutional neural operators for robust and accurate learning of pdes. *Advances in Neural Information Processing Systems*, 2023a.
- Raonic, B., Molinaro, R., Rohner, T., Mishra, S., and de Bezenac, E. Convolutional neural operators. In *ICLR 2023 Workshop on Physics for Machine Learning*, 2023b.
- Rashid, M. M., Pittie, T., Chakraborty, S., and Krishnan, N. A. Learning the stress-strain fields in digital composites using fourier neural operator. *Isience*, 25(11), 2022.

- Rumelhart, D. E., Hinton, G. E., and Williams, R. J. Learning representations by back-propagating errors. *nature*, 323(6088):533–536, 1986.
- Shin, J. Y., Lee, J. Y., and Hwang, H. J. Pseudo-differential neural operator: Generalized fourier neural operator for learning solution operators of partial differential equations. *ArXiv*, abs/2201.11967, 2022.
- Takamoto, M., Praditia, T., Leiteritz, R., MacKinlay, D., Alesiani, F., Pflüger, D., and Niepert, M. Pdebench: An extensive benchmark for scientific machine learning. *Advances in Neural Information Processing Systems*, 2022.
- Tiwari, K., Krishnan, N., et al. Cono: Complex neural operator for continuous dynamical systems. *ArXiv*, abs/2310.02094, 2023.
- Tiwari, K., Dutta, N., Krishnan, N. A., and AP, P. Latent mamba operator for partial differential equations. In *Proceedings of the 42nd International Conference on Machine Learning*, 2025.
- Wang, H., Fu, T., Du, Y., Gao, W., Huang, K., Liu, Z., Chandak, P., Liu, S., Van Katwyk, P., Deac, A., et al. Scientific discovery in the age of artificial intelligence. *Nature*, 620(7972):47–60, 2023.
- Wen, G., Li, Z., Azizzadenesheli, K., Anandkumar, A., and Benson, S. M. U-fno—an enhanced fourier neural operator-based deep-learning model for multiphase flow. *Advances in Water Resources*, 163:104180, 2022.
- Wigner, E. On the quantum correction for thermodynamic equilibrium. *Physical review*, 40(5):749, 1932.
- Wu, H., Hu, T., Luo, H., Wang, J., and Long, M. Solving high-dimensional pdes with latent spectral models. In *Proceedings of the 40th International Conference on Machine Learning*, 2023.
- Wu, H., Luo, H., Wang, H., Wang, J., and Long, M. Transolver: A fast transformer solver for pdes on general geometries. In *Proceedings of the 41st International Conference on Machine Learning*, 2024a.
- Wu, H., Weng, K., Zhou, S., Huang, X., and Xiong, W. Neural manifold operators for learning the evolution of physical dynamics. In *Proceedings of the 30th ACM SIGKDD Conference on Knowledge Discovery and Data Mining*, pp. 3356–3366, 2024b.
- Xiao, Z., Hao, Z., Lin, B., Deng, Z., and Su, H. Improved Operator Learning by Orthogonal Attention. In *Proceedings of the 41st International Conference on Machine Learning*, 2024.
- Zhang, E., Kahana, A., Kopaničáková, A., Turkel, E., Ranade, R., Pathak, J., and Karniadakis, G. E. Blending neural operators and relaxation methods in pde numerical solvers. *Nature Machine Intelligence*, pp. 1–11, 2024.

A. Table of Notations

A table of key notations is given in Table 6.

B. Model, Experiment Settings and Results

Differential Operator We compensate for possible local information lost by propagating the finite difference derivative of x on the local region:

$$\mathcal{K}_{L-1}[v_{L-1}](x, p) = \frac{\iint_{D_{loc} \times D_p} \kappa_{L-1}(x, y, p, p')(v_{L-1}(y, p') - v_{L-1}(x, p')) dy dp'}{\iint_{D_{loc} \times D_p} \kappa_{L-1}(x, y)(y - x, p') dy dp'}, \quad (15)$$

where $D_{loc} \subset D_x$ denotes the local region around the query position x . In this work, the implementation of Equ.15 is based on the convolution layer in (Liu-Schiaffini et al., 2024). Related ablation results see Tab.3 and Tab.16.

Loss Denote the parameterized neural operator as \mathcal{G}_θ , we aim to approximate the solution operator \mathcal{G} in Equation 10 by optimizing the model parameters $\theta \in \Theta$ through relative L_2 loss below:

$$\min_{\theta \in \Theta} \mathcal{L}(\theta) := \min_{\theta \in \Theta} \frac{1}{S} \sum_{s=1}^S \left[\frac{\|\mathcal{G}_\theta[a_s] - u_s\|_2}{\|u_s\|_2} \right] \quad (16)$$

$$= \min_{\theta \in \Theta} \frac{1}{S} \sum_{s=1}^S \left[\left(\frac{\sum_j (\mathcal{G}_\theta[a_s](x_j) - u_s(x_j))^2}{\sum_j (u_s(x_j))^2} \right)^{\frac{1}{2}} \right], \quad (17)$$

where Θ , S , and $u_s = u_s(x)$ denote the parameter space, the number of function samples, and the i -th output function, respectively.

Benchmarks and Results Benchmarks and the corresponding experimental results are summarized below:

1. 1D Heat Equation

Consider the 1D Heat Equation as follows:

$$\partial_t u = c \partial_{xx} u, \quad (18)$$

where $c = 0.05$ as in (Shin et al., 2022). We generate 1200 samples (1000 for the training set, and 100 for testing) in a denser grid with size $2^{10} = 1024$, and down-sample them to size $2^8 = 256$. Our goal is to predict solution $u_1 = u(x, t = 1)$ from $u_0 = u(x, t = 0)$. Results are shown in Tab.1.

2. 1D Advection Equation

Consider 1D Advection Equation:

$$\partial_t u = \beta \partial_x u, \quad (19)$$

where β is set with 1. We use the data from (Takamoto et al., 2022) with 2000 samples of $u_0 = u(x, t = 0)$. Our goal is to predict the next 10 time steps from the last 10 of the solution $u(x, t)$. The number of training and testing samples is 1000 and 200, respectively. Results are shown in Tab.1

3. 1D Burgers Equation

The 1D Burger’s Equation on the unit torus is formed as (Li et al., 2021):

$$\partial_t u + u \partial_x u = \nu \partial_{xx} u, \quad (20)$$

where $\nu = 0.1$ with periodic boundary conditions. Our goal is to build a solution operator to predict the solution $u(x)$ at $t = 1$. The training and testing grid size is set with $2^7 = 128$. Results are listed in Tab.2.

4. 2D Gray-Scott System

Consider a pair of coupled reaction-diffusion PDEs as follows:

$$\begin{aligned}\partial_t u &= D_u \Delta u - uv^2 + F(1 - u), \\ \partial_t v &= D_v \Delta v - uv^2 - (F + k)v,\end{aligned}\tag{21}$$

where $D_u = 0.2097$, $D_v = 0.105$ denote the diffusion coefficients respectively for u, v . And $F = 0.03$, $k = 0.062$ are the reaction parameters. We follow the data generation in (Kassai Koupai et al., 2024) to make a training set with 200 samples of u, v evolution and a testing set with 20 in a 32×32 size grid with periodic boundary conditions. Our goal is to predict the next 10 time steps from the last 10 of u, v . See Tab.2 for results.

5. 2D Shallow-Water Equations

The 2D shallow-water equations govern the evolution of fluid flows under the assumption that horizontal length scales are much larger than the vertical depth. They can be expressed as the following system of hyperbolic PDEs:

$$\partial_t h + \nabla h \mathbf{u} = 0,\tag{22}$$

$$\partial_t h \mathbf{u} + \nabla \left(\mathbf{u}^2 h + \frac{1}{2} g_r h^2 \right) = -g_r h \nabla b,\tag{23}$$

where $h = h(x, t)$ denotes the fluid depth, $\mathbf{u} = \mathbf{u}(x, t)$ is the 2D velocity field, g_r is the (reduced) gravitational acceleration, $b = b(x)$ represents the bathymetry characterizing the bottom topography. For this benchmark, we employ the dataset from (Takamoto et al., 2022), which is generated under Neumann boundary conditions. To assess resolution-invariant stability during training, models are trained on 500 samples with resolutions randomly drawn from $\{32, 64, 128\}$ and evaluated on 300 test samples at the highest resolution 128. The prediction task is to forecast the water depth over the next 10 time steps, given the previous 10. See Tab.13 for results.

6. 2D Darcy Flow

The 2D Darcy Flow is a second-order elliptic equation as follows:

$$-\nabla \cdot (a \nabla u) = f,\tag{24}$$

where $f = 1$. Our goal is to approximate the mapping operator from the coefficient distribution function $a(x)$ to the solution function $u(x)$ with zero Dirichlet boundary conditions (Li et al., 2021). The results are based on models trained on 1000 training samples, which are down-sampled to a size of (85×85) , and tested on 100 samples. Results are listed in Tab.13.

7. 2D Incompressible Navier-Stokes Equations

The 2D incompressible Navier-Stokes (NS) Equations in vorticity form on a unit torus are shown below:

$$\partial_t \omega + u \cdot \nabla \omega - \nu \Delta \omega = f,\tag{25}$$

$$\nabla \cdot u = 0.\tag{26}$$

Here $\nu = 1e-5$ and $f = 0.1(\sin(2\pi(x_1 + x_2)) + \cos(2\pi(x_1 + x_2)))$. Our goal is to predict the next 10 time steps from the last 10 ($d_a = d_u = 10$) of the solution $w(x, t)$ with periodic boundary conditions on the 2D grid with size 64×64 (Li et al., 2021). All models in Table 2 are trained on 1000 training samples and tested on 200 test samples. Results are listed in Tab.2.

8. 3D Compressible Navier-Stokes Equations

The 3D compressible NS equations describe fluid dynamics with density changes, given by:

$$\partial_t \rho + \nabla \cdot (\rho \mathbf{v}) = 0,\tag{27}$$

$$\rho(\partial_t \mathbf{v} + \mathbf{v} \cdot \nabla \mathbf{v}) = -\nabla p + \eta \Delta \mathbf{v} + (\zeta + \eta/3) \nabla(\nabla \cdot \mathbf{v}),\tag{28}$$

$$\partial_t \left[\epsilon + \frac{\rho v^2}{2} \right] + \nabla \cdot \left[\left(\epsilon + p + \frac{\rho v^2}{2} \right) \mathbf{v} - \mathbf{v} \cdot \sigma' \right] = 0,\tag{29}$$

where $\mathbf{v} = \mathbf{v}(x, t)$, $\rho = \rho(x, t)$, and $p = p(x, t)$ denote the velocity vector field, fluid density (mass per unit volume), and pressure, respectively. We consider the challenging transonic flow benchmark from (Takamoto et al., 2022), with shear and bulk viscosity coefficients $\eta = \zeta = 1 \times 10^{-8}$, and internal energy density $\epsilon = \frac{3p}{2}$. The viscous stress tensor $\sigma' = \sigma'(\mathbf{v}; \eta, \zeta)$ is determined by the velocity field under the Newtonian fluid assumption. Our objective is to predict the velocity, density, and pressure fields three time steps ahead, given the previous three steps ($d_a = d_u = 3 \times 5 = 15$). The simulations are performed on a downsampled 3D grid of size $32 \times 32 \times 32$ with periodic boundary conditions. The initial conditions consist of turbulent velocity fields with uniform mass density and pressure. All benchmark models are trained on 500 samples and evaluated on 100 test samples. See Tab.13 for results.

9. 3D Rayleigh-Taylor Instability

The Rayleigh–Taylor (RT) instability occurs when a heavier fluid overlies a lighter one under the influence of gravity, which is extremely sensitive to perturbations of the interface and governed by the following PDEs:

$$\partial_t \rho + \nabla \cdot (\rho \mathbf{u}) = 0, \quad (30)$$

$$\partial_t (\rho \mathbf{u}) + \nabla \cdot (\rho \mathbf{u} \mathbf{u}) = -\nabla p + \nabla \cdot \boldsymbol{\tau} + \rho \mathbf{g}, \quad (31)$$

$$\nabla \cdot \mathbf{u} = -\kappa \nabla \cdot \left(\frac{\nabla \rho}{\rho} \right). \quad (32)$$

where $\rho = \rho(x, t)$ and $\mathbf{u} = \mathbf{u}(x, t)$ denote the density and the velocity vector field, respectively. p is the pressure, $\boldsymbol{\tau} = \boldsymbol{\tau}(\mathbf{u}, \rho; \nu)$ is the eviatoric stress tensor with kinematic viscosity ν , \mathbf{g} represents the gravity, and κ is the coefficient of molecular diffusivity. A key dimensionless parameter in the RT simulations is the Atwood number $A = (\rho_h - \rho_l) / (\rho_h + \rho_l)$, which quantifies the density contrast between the two fluids. For example, miscible fluids with greater density contrasts exhibit stronger instabilities. In this work, we adopt the dataset with $A = 0.25$ provided in (Ohana et al., 2024) to train a solution operator $vec(\rho, \mathbf{u}; t = t_0) \mapsto vec(\rho, \mathbf{u}; t = t_0 + 20)$ which evolves the system from rest states (with small perturbations) to mixed states after 20 time steps. The models are trained on 220 mapping pairs and tested on 40 pairs from distinct trajectories, using a downsampled grid of size $32 \times 32 \times 32$. Horizontal periodic boundary conditions and impermeable vertical walls are imposed. See Tab.2 for results.

10. ERA5 Wind Field Prediction

To compare the baseline models in a global context of spatio-temporal dynamics, we evaluate their performance on predicting the next-hour ERA5 global wind field (Hersbach et al., 2020). All models are trained using data from the previous four days to predict the next-hour wind field at a grid size of 512×512 , and are tested on data from a new day with the same grid size. See Tab.15 for results.

We emphasize the broader learning difficulty spectrum of the benchmarks we selected. As shown in Fig. 5 (Li et al., 2021) which illustrates the spectral decay of truncation modes, our chosen benchmarks 6 and 7 contain significantly more high-frequency modes than simpler benchmarks such as 3 or other incompressible NS benchmarks with $\nu > 1 \times 10^{-4}$. To further evaluate the capability of these efficient and lightweight neural operators in capturing complex non-linear dynamics in 3D space, we include two additional, extremely challenging benchmarks: 8 and 9. Moreover, we also compare the performance of all baseline models in the rapid prediction of global wind fields, providing a comprehensive evaluation across both highly nonlinear and large-scale spatio-temporal dynamics.

Baselines The principle of our experiment configurations for different baselines is to keep the best configuration provided in their papers or codes, while ensuring fairness and not exploding the *Nvidia GeForce RTX 4090* GPU memory (limited to 24564MiB). Detailed configurations of all baselines in different experiments are shown in Table 7. And some explanation notes are listed below:

- Mainly two types of Positional Features (Pos. Feat.), absolute coordinates (Abs.) and reference grid (Ref.), are concatenated into input signals: (1) FNO (Li et al., 2021) concatenates the input function value $a \in \mathbb{R}^{d_a}$ with the normalized absolute position coordinate $x \in \mathbb{R}^d$, usually scaled between 0 and 1. (2) Transolver (Wu et al., 2024a), on the other hand, uses an advanced version which constructs a coarse reference grid and computes Euclidean distances from each input point to each point in this reference grid, concatenating these relative positions $x_{ref} \in \mathbb{R}^{(d_{ref})^d}$. In our work, we utilize the same absolute positional features as FNO to ensure a fair comparison.

- Since Transolver employs the multi-head in its implementation, it creates sub-grid with a equal size from the complete one.
- For Transolver, the optimizers and scheduler type is AdamW (Loshchilov & Hutter, 2019) and OneCycleLR, while for FNO and SKNO are Adam (Kingma & Lei Ba, 2015) and Cosine Annealing. All the learning rates are initially set to 0.001. More configurations can be found in the code provided in our supplementary materials.

Zero-shot Super-resolution To assess the resolution-invariant inference capability of SKNO, we evaluate the model on three benchmarks: 1D Burgers’ equation (trained on a grid of size 128), 2D Darcy Flow (trained on a grid of size 85×85), and ERA5 Global Wind Field Prediction (trained on a grid of size 32×32). As shown in Tab. 12 and Tab. 14, SKNO maintains stability and accuracy even when tested on extremely fine grids, including 8192 , $(421)^2$, and $(512)^2$. All experiments are conducted on a single RTX 4090 GPU, consistent with the setup used in other sections.

Averaging Neural Operator on D_p In experiments governed by non-linear equations, we utilize $F_p^{-1}\tilde{A}F_p + B$, where \tilde{A} and B are both matrices with diagonally enhanced initialization. Such kind of implementation can be thought as an Averaging Neural Operator (ANO) (Lanthaler et al., 2025) along p , which governs the universal approximation of the PDE operator on D_p .

C. Related Work

Adding one dimension to solve PDEs Unlike traditional methods (Lucia et al., 2004; Chinesta et al., 2011) that rely on dimension reduction techniques, such as symmetry analysis (Cantwell, 2002), to represent equations within their original domain, approaches like the level set method (Osher & Fedkiw, 2001; Osher et al., 2004; Adalsteinsson & Sethian, 1995; Jin & Osher, 2003) and the recent Schrödingerisation method (Jin & Liu, 2024; Jin et al., 2023; 2024) propose extending original PDEs to one more higher dimensional domains to create a pipe for functions to evolve. Similar "adding one dimension" ideas have also been used in signal processing like wavelets (Meyer, 1992) which employ scale and shift dimensions to represent original signals, and in quantum mechanics like the Wigner functions (Wigner, 1932) which utilize a single function displaying the probability (quasi-)distribution in the phase space.

Neural Networks for PDEs In scenarios where PDEs are unknown or training data is limited, supervised learning methods are employed to approximate solution operators, which recently shows their capacity to universally represent solution operators for partial differential equations (PDEs) (Hornik et al., 1989; Kovachki et al., 2021; Lu et al., 2021; Lagaris et al., 1998). Existing approaches mainly fall into two paradigms: Common Neural Networks and Neural Operators.

Common NNs approximate solution operators working on a fixed grid size, which maps discretized input to output signals using architectures such as MLPs (He et al., 2016; Chen et al., 2018), CNNs (Qu et al., 2022; Brandstetter et al., 2023). For example, (Obiols-Sales et al., 2020; Khoo et al., 2021) utilizes a typical CNN structure to map the input to the output image, which is composed of the solution of numerical solvers.

Neural operators (NOs) are designed to map between function spaces, enabling generalization across varying input discretizations without retraining (Kovachki et al., 2023; Wang et al., 2023). One of the most popular NO definitions is the kernel integral operator (Li et al., 2021; Raonic et al., 2023b; Cao et al., 2024). Early kernel function implementations employed graph-based message-passing networks (Li et al., 2020a;b), where dense edge connections encoded these kernels. However, these methods faced scalability challenges due to long training times and inefficiencies in modeling interactions across multiple spatial and temporal scales. Transformer-based models (Kissas et al., 2022), similar to graphs, also encounter limitations in computational efficiency due to quadratic time complexity. To address these challenges, tricky computation strategies on kernels have been proposed. Galerkin-based methods (Cao, 2021; Ern & Guermond, 2004) employ linear projections to parameterize kernels, while (Xiao et al., 2024) introduces a decomposition constrained by positive semi-definite assumptions. However, such methods suffer from the problems of reduced expressiveness due to the absence of non-linear activations like softmax. Recent SOTA model transolver (Wu et al., 2024a) proposes a physics-attention module to approximate the kernel function with the aid of a self-attention-based aggregation on flattened data. While these graph or transformer-based advanced methods try to escape from the heavy quadratic complexity by tricky implementations on the kernel functions originally defined in (Li et al., 2020a; 2021), they still pay the computational price for their neglect of the framework and model alignment in embedding spaces. While Mamba-based methods such as (Tiwari et al., 2025) can further reduce the computational cost over the domain after aggregation, the representational and complexity bottlenecks in

the embeddings remain unaddressed. Instead, empirically designed fully connected or multi-head architectures are typically retained by default to model the evolution along the auxiliary dimension.

Additionally, Fourier Neural Operators (FNO) (Li et al., 2021) efficiently implement spectral kernel representations by global convolutions via the Fast Fourier Transform (FFT). While training fast, it also faces the representation bottleneck like other NO methods because of the unaligned evolution in embedding spaces. Subsequent works take efforts to extend the Fourier Transform to other analytically well-explored transformations. For example, Complex Neural Operator (Tiwari et al., 2023) generalizes the Fourier Transformation with an extra learnable rotation parameter to model the d -dimensional kernel integration.

There is another NO definition: DeepONet (Lu et al., 2021) employs a branch-trunk architecture inspired by the universal operator approximation theorem (Chen & Chen, 1995). These representations are combined through a dot product for the embeddings composed with functional outputs to predict the solution values. Recent advancements, such as integrating numerical solvers with DeepONet (Zhang et al., 2024), have improved convergence by capturing multi-frequency components, enhancing performance on complex PDE systems. However, its general-purpose design may limit its effectiveness in scenarios requiring high accuracy and PDE-aligned structural representations.

D. Properties of SKNO

We highlight several properties of SKNO below.

Complexity To analyze computational complexity across general dimensional settings (1D, 2D, 3D, ...), let N_x denote the number of grid points in the spatial domain, N_p the grid size along the auxiliary dimension, and k_x the number of aggregated slices/nodes (used in Transolver). The complexity comparison is summarized in Tab. 8.

Table 8. Complexity comparison of different kernel implementations.

Models	Complexity
Transolver	$\mathcal{O}[N_p(N_x(k_x + N_p) + k_x^2)]$ ($k_x \geq 32$, $N_p = 128$ or 256)
FNO	$\mathcal{O}[N_p(N_x \log(N_x) + N_p k_x)]$ ($k_x \leq 16$, $N_p \leq 32$)
SKNO (Ours)	$\mathcal{O}[N_p(N_x(\log N_x + \log N_p) + N_p k_x)]$ ($k_x \leq 16$, $N_p \leq 32$)

Table 9. Complexity comparison of different lifting implementations with positional encoding. (Assume all choose one linear layer)

Models	Complexity
Transolver	$\mathcal{O}[N_p(d_a + (d_{ref})^d)]$ ($d_{ref} = 8$, $N_p = 128$ or 256)
FNO	$\mathcal{O}[N_p(d_a + d)]$ ($N_p \leq 32$)
SKNO (Ours)	$\mathcal{O}[N_p(d_a + d)]$ ($N_p \leq 32$)

Consider an extreme but practically relevant case in high-accuracy numerical simulations: a 3D field with grid resolution $((2)^9)^3 = (512)^3$ and $N_p = 32$ (while Transolver typically requires $N_p = 128$ for stable performance). Even with the minimal $k_x = 32$, Transolver’s kernel implementation with a large linear constant ($k_x + N_p > 128$) leads to a computational cost much higher than SKNO ($\log N_x = 27$) or FNO ($\log N_x N_p = 27 + 5 = 32$).

In lower dimensions like 1D or 2D cases, where N_x is exponentially smaller, our kernel retains the linear-complexity advantages while achieving superior performance with significantly smaller scale constants compared to the SOTA Transolver (under the log benefit from Fast Fourier Transform). Here, we report the FLOPs of the kernel integration on representative experiments in Tab. 10. Notably, when the positional encodings are removed in Table 9, the prediction error of Transolver increases dramatically (from $6e - 3$ to $6e - 1$ in relative L_2 error on Burgers), whereas the other two models maintain nearly the same accuracy level.

Table 10. Computational cost comparison (FLOPs) of the kernel integration and relative rate (normalized by FNO).

Model \ Metric	FNO	Transolver	SKNO
<i>2D Navier–Stokes</i>			
FLOPs	1.16×10^8	1.19×10^9	2.12×10^8
Rate	1.000	10.292	1.831
<i>3D Rayleigh–Taylor Instability</i>			
FLOPs	8.98×10^8	9.00×10^9	1.59×10^9
Rate	1.000	10.029	1.774

Spectral Operator along p Since our SKNO adopts a spectral implementation, we primarily compare it to the FNO (Li et al., 2021) as a reference framework. This choice also facilitates generalization to other spectral models like (Guibas et al., 2022; Li et al., 2024). To avoid notational clutter, we begin with the $d = 1$ case, noting that the following arguments extend straightforwardly to higher dimensions.

Theorem D.1 (Neural Operator along the Auxiliary Dimension). *Let $v(x, p)$ be taken from a compact set V in the appropriate Sobolev space so that its truncated Fourier representatives*

$$\hat{v}_i := F_{k_x}^x [P_{k_x}^x v](\hat{\mathbf{x}}_i, \mathbf{p}) \in \hat{V}_i \subset \mathbb{C}^{N_p}, \quad \tilde{v}_i := F^p [R_{k_p}^p (F_{k_x}^x [P_{k_x}^x v])](\hat{\mathbf{x}}_i, \tilde{\mathbf{p}}) \in \tilde{V}_i \subset \mathbb{C}^{N_p},$$

are compact sets in a finite coefficient space. Then

1. Approximating an operator \mathcal{M} is equivalent (via the Fourier-conjugate decomposition) to approximating the conjugate mapping(s) $\{\widehat{\mathcal{M}}_i\}_{i=1}^{k_x}$ (and, after also Fourier-transforming in p , the conjugates $\{\widetilde{\mathcal{M}}_i\}$).
2. The forward DFT/frequency-projection and the inverse discrete transform admit neural operator approximation on the spectral domain (See Lemma 7 and Lemma 8 in (Kovachki et al., 2021)), hence the operator learning problem reduces to a finite-dimensional neural-network approximation on the compact coefficient sets \hat{V}_i, \tilde{V}_i .

In particular, treating the auxiliary p -dimension via an additional DFT (as SKNO does) simply produces an enlarged conjugate mapping; the same approximation strategy (as Lemma 7 + Lemma 8 + finite NN on compact coefficients) applies.

Note. $\widehat{\mathcal{M}}_i : \hat{V}_i \subset \mathbb{R}^{2N_p} \rightarrow \mathbb{R}^{2N_p}$ for $i = 1, \dots, k_x$ and $\widetilde{\mathcal{M}}_i : \tilde{V}_i \subset \mathbb{R}^{2N_p} \rightarrow \mathbb{R}^{2N_p}$. Usually, we take $k_p = N_p$ and the $\frac{\text{length}(\mathbf{p}) - k_p}{\text{length}(\mathbf{p})}$ random dropout $R_{k_p}^p = I^p$.

Proof. By the Fourier-conjugate decomposition (Eq. (12) in (Kovachki et al., 2021)), the operator can be written as

$$\begin{aligned} \mathcal{M} &= (F_{k_x}^x)^{-1} \circ \widehat{\mathcal{M}}_{k_x} \circ F_{k_x}^x \circ P_{k_x}^x \\ &= (F_{k_x}^x)^{-1} \circ (F^p)^{-1} \circ \widetilde{\mathcal{M}}_{k_x} \circ F^p \circ F_{k_x}^x \circ P_{k_x}^x. \end{aligned} \quad (33)$$

Here, the second line follows from additionally applying a DFT in the auxiliary variable p .

The mapping in Equ.33 $F^p F_{k_x}^x [P_{k_x}^x (\cdot)]$ sends the compact input family V into a compact subset of Fourier coefficient space.

Lemma 7 and Lemma 8 of (Kovachki et al., 2021) guarantee that the left-hand and right-hand parts of both $\widehat{\mathcal{M}}_{k_x}$ and $\widetilde{\mathcal{M}}_{k_x}$ can be approximated within the desired accuracy.

Thus, the problem reduces to approximating the conjugate operators $\widehat{\mathcal{M}}_{k_x}$ or $\widetilde{\mathcal{M}}_{k_x}$, both of which are continuous maps defined on compact subsets of \mathbb{R}^{2N_p} . By the universal approximation theorem for neural networks (Barron, 2002; Hornik

et al., 1989), any such continuous map can be approximated to arbitrary accuracy by a finite neural network. Hence, there exists finite NNs that approximate the conjugate mappings on \hat{V}_i (or \tilde{V}_i) within the desired accuracy.

Easy to show that SKNO universally approximates any d -dimensional operator, see Theorem 5 in (Kovachki et al., 2021).

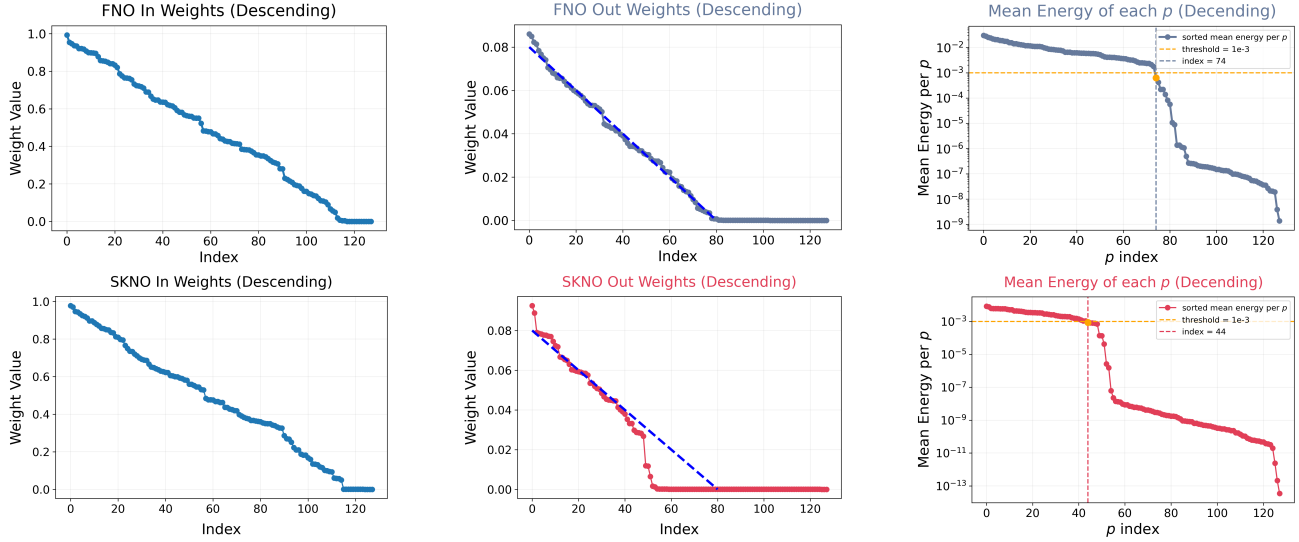


Figure 6. Dictionary comparison of FNO and SKNO. We train both models with a sufficiently large recovering budget N_p on the Burgers benchmark and visualize the absolute values of the input/output weights, together with the mean energy of the dictionary of pattern fields. While the input weights of FNO (top left) and SKNO (bottom left) exhibit nearly identical distributions, SKNO yields a noticeably sparser structure in its output weights (bottom middle) and in the mean energy of each pattern field (bottom right) compared to FNO. The yellow horizontal line denotes a mean-energy threshold of 10^{-3} , where modes below this threshold contribute only marginally to the final prediction. For a complete visualization of the output-weight and pattern-field pairs in the dictionary, see Fig. 16.

Sparsity Due to the limited network width, N_p should be finite and as small as possible. Benefiting from the PDE-aligned propagator design, SKNO constructs a sparser dictionary on the output side of the $d + 1$ dimensional propagation pipes that is more efficient in capturing the energy of the solutions than FNO.

For a clear and fair comparison, we consider SKNO without the differential operator and the baseline FNO. The lifting and recovering operators in both models are chosen as unbiased linear layers without positional encoding. Under the same configurations, we compare the dictionaries of SKNO and FNO at the last output linear layer in Fig.6, which illustrates the sparsity advantage of the SKNO dictionary.

Beyond the experiments, we also provide a formal proof in a finite-dimensional matrix–vector setting, which aligns well with the neural implementation, to clarify the efficient energy capture of SKNO. The extension to function spaces amounts to working in the corresponding infinite-dimensional setting.

Lemma D.2 (Preserved Energy after Top- r Truncation). *For a general matrix–vector multiplication $\mathbf{u} = G\mathbf{y}$ where $G \in \mathbb{R}^{N_x \times N_p}$ and $N_x \geq N_p$, if we perform the top- r approximation G_r using the singular value decomposition (SVD) of G , the energy preserved in the prediction $G_r\mathbf{y}$ is*

$$\|G_r\mathbf{y}\|_2^2 = \sum_{m=1}^r \lambda_m^2 \langle \mathbf{y}, \phi_m \rangle^2, \quad r \leq N_x, \quad (34)$$

where $G_r\mathbf{y} = \Psi_r \Lambda_r \Phi_r^T \mathbf{y} = \sum_{m=1}^r \lambda_m \langle \mathbf{y}, \phi_m \rangle \psi_m$, and ψ_m , ϕ_m , and λ_m are the m -th left singular vector, right singular vector, and singular value, respectively.

Proof. This follows directly from $G_r\mathbf{y}$ representing with the orthonormal basis $\{\psi_m\}$ of $\text{range}(r)$.

Theorem D.3 (Efficient Energy Capture with Limited Width $r < N_p$). *Assuming the models have the same \mathcal{P} , we have*

$$\left\| u(x) - \sum_{m=1}^r \chi_m^{(\text{FNO})} (v_L)_m^{(\text{FNO})} (x) \right\|_2 - \left\| u(x) - \sum_{m=1}^r \chi_m^{(\text{SKNO})} (v_L)_m^{(\text{SKNO})} (x) \right\|_2 = \|u(x)\|_2 \cdot \epsilon(r), \quad (35)$$

where $\epsilon(r)$ is a non-increasing function with respect to r . When $r \rightarrow N_p$, $\epsilon(r) \rightarrow 0$.

Note. (1) The length N_x in the following discussion is obtained by flattening the d -dimensional tensor while keeping the sequential order. (2) Without loss of generality, we discuss the case $d_u = 1$.

Proof. Denote the vector $\mathbf{u} \in \mathbb{R}^{N_x}$ discretized on D_x , the vector $\boldsymbol{\chi}^{(M)} \in \mathbb{R}^{N_p}$ discretized on N_p , the matrix $V_L^{(M)} \in \mathbb{R}^{N_x \times N_p}$ where $N_x \geq N_p$. We focus on the last output (linear) layer in neural operators M. If N_p is sufficiently large, we have

$$\begin{aligned} \mathbf{u} &= V_L^{(M)} \boldsymbol{\chi}^{(M)} \\ &= \Psi_L^{(M)} \Lambda_L^{(M)} (\Phi_L^{(M)})^T \boldsymbol{\chi}^{(M)}, \end{aligned} \quad (36)$$

with singular values $\lambda_1^{(M)} \geq \lambda_2^{(M)} \geq \dots \geq \lambda_{N_x}^{(M)}$. The matrices $\Psi_L^{(M)} = (\psi_1^{(M)}, \psi_2^{(M)}, \dots, \psi_{N_x}^{(M)})$ and $\Phi_L^{(M)} = (\phi_1^{(M)}, \phi_2^{(M)}, \dots, \phi_{N_p}^{(M)})$ are composed with their column vectors $\{\psi_m\}_{m=1}^{N_x}$ and $\{\phi_m\}_{m=1}^{N_p}$, respectively.

In practice, we apply the r -truncation on N_p as the optimal approximation under the metric in Equ. 16. Utilizing the rank- r truncated SVD, we have

$$\begin{aligned} (V_L^{(M)})_r &:= (\Psi_L^{(M)})_r (\Lambda_L^{(M)})_r (\Phi_L^{(M)})_r^T \\ &= \sum_{m=1}^r \lambda_m^{(M)} \psi_m^{(M)} (\phi_m^{(M)})^T, \quad r \leq N_x. \end{aligned} \quad (37)$$

From Lemma D.2, the (relative) energy of u captured by the top- r SVD modes of model M is

$$\begin{aligned} E^{(M)}(r) &:= \frac{\|(V_L^{(M)})_r \boldsymbol{\chi}^{(M)}\|_2^2}{\|\mathbf{u}\|_2^2} \\ &= \frac{\sum_{m=1}^r (\lambda_m^{(M)})^2 \langle \boldsymbol{\chi}^{(M)}, \phi_m^{(M)} \rangle^2}{\sum_{m=1}^{N_x} (\lambda_m^{(M)})^2 \langle \boldsymbol{\chi}^{(M)}, \phi_m^{(M)} \rangle^2}. \end{aligned} \quad (38)$$

Since singular values are non-negative, the sequence $E^{(M)}(r)$ is non-decreasing with respect to r for each model M. And the truncation error is

$$\|\mathbf{u} - (V_L^{(M)})_r \boldsymbol{\chi}^{(M)}\|_2 = \|\mathbf{u}\|_2 \sqrt{1 - E^{(M)}(r)}, \quad r = 1, \dots, N_x. \quad (39)$$

Specifically, the error difference between FNO and SKNO is

$$\begin{aligned} \epsilon(r) &= \frac{\|\mathbf{u} - (V_L^{(\text{FNO})})_r \boldsymbol{\chi}\|_2 - \|\mathbf{u} - (V_L^{(\text{SKNO})})_r \boldsymbol{\chi}\|_2}{\|\mathbf{u}\|_2} \\ &:= \sqrt{1 - E^{(\text{FNO})}(r)} - \sqrt{1 - E^{(\text{SKNO})}(r)}. \end{aligned} \quad (40)$$

From Equ.38, $\epsilon(r) \rightarrow 0$ as $r \rightarrow N_p$.

Let $\mathcal{H}^{(M)}$ denotes the set of $V_L^{(M)}$ that can be realized by NO M under the same width budget r . We have

$$E^{(M)}(r) := \sup_{V_L^{(M)} \in \mathcal{H}_M} \frac{\|(V_L^{(M)})_r \boldsymbol{\chi}^{(M)}\|_2^2}{\|\mathbf{u}\|_2^2}, \quad M \in \{\text{FNO}, \text{SKNO}\}, \quad r \leq N_p. \quad (41)$$

Since $\mathcal{H}_{\text{FNO}} \subset \mathcal{H}_{\text{SKNO}}$, the supremum over $\mathcal{H}_{\text{SKNO}}$ cannot be smaller than the supremum over \mathcal{H}_{FNO} , which implies

$$E^{(\text{SKNO})}(r) \geq E^{(\text{FNO})}(r), \forall r \leq N_p. \quad (42)$$

Thus, for all $r = 1, \dots, N_p$

$$\epsilon(r) \geq 0, \quad (43)$$

It is straightforward to extend the above arguments to function spaces.

Adjoint Backward Propagation Under the squared loss function like Equ. 16, we show the adjoint backward propagation property of SKNO.

Theorem D.4 (Backward Residual Propagation). *Here we show the backward updates around linear kernel integrations in SKNO. Assume $d_a = d_u = 1$ and denote the matrix multiplication on the last output layer $V_L^{(\text{SKNO})} \chi^{(\text{SKNO})}$ and the backward input residual $\mathbf{r}^{(\text{SKNO})}$, where the vector $\chi^{(\text{SKNO})} \in \mathbb{R}^{N_p}$ is discretized on N_p , and the matrix $V_L^{(\text{SKNO})} \in \mathbb{R}^{N_x \times N_p}$ where $N_x > N_p$. The backpropagation (Rumelhart et al., 1986) update*

$$\Delta \chi^{(\text{SKNO})} = \sum_i (V_L^{(\text{SKNO})})_i^T \cdot \mathbf{r}_i^{(\text{SKNO})} \quad (44)$$

$$\text{Grad}(V_L^{(\text{SKNO})}) = \mathbf{r}^{(\text{SKNO})} \cdot (\chi^{(\text{SKNO})})^T \quad (45)$$

$$FC : (\Delta \hat{\mathbf{B}})_{ijj'} = \text{conj}(\hat{V}_{L-1})_{ij} \cdot \hat{\mathbf{r}}_i^{(\text{SKNO})} \cdot \mathbf{M}_{ij'}^{(\text{SKNO})} \cdot (\chi^{(\text{SKNO})})_{j'}^T \quad (46)$$

$$\text{Grad}(\hat{V}_{L-1}^{(\text{SKNO})})_{ij} = \sum_{j'} \hat{\mathbf{B}}_{ijj'} \cdot \hat{\mathbf{r}}_i^{(\text{SKNO})} \cdot \mathbf{M}_{ij'}^{(\text{SKNO})} \cdot (\chi^{(\text{SKNO})})_{j'}^T \quad (47)$$

$$(\Delta \hat{\mathbf{A}})_{ijj'} = \text{conj}(\hat{V}_{L-1})_{ij} \cdot \hat{\mathbf{r}}_i^{(\text{SKNO})} \cdot \mathbf{M}_{ij'}^{(\text{SKNO})} \cdot (\tilde{\chi}^{(\text{SKNO})})_{j'}^T \quad (48)$$

$$\text{Grad}(\hat{V}_{L-1}^{(\text{SKNO})})_{ij} = \sum_{j'} \hat{\mathbf{A}}_{ijj'} \cdot \hat{\mathbf{r}}_i^{(\text{SKNO})} \cdot \mathbf{M}_{ij'}^{(\text{SKNO})} \cdot (\tilde{\chi}^{(\text{SKNO})})_{j'}^T \quad (49)$$

$$\text{Diag} : (\Delta \hat{\mathbf{B}})_{ij} = \text{conj}(\hat{V}_{L-1})_{ij} \cdot \hat{\mathbf{r}}_i^{(\text{SKNO})} \cdot \mathbf{M}_{ij}^{(\text{SKNO})} \cdot (\chi^{(\text{SKNO})})_j^T \quad (50)$$

$$\text{Grad}(\hat{V}_{L-1}^{(\text{SKNO})})_{ij} = \hat{\mathbf{B}}_{ij} \cdot \hat{\mathbf{r}}_i^{(\text{SKNO})} \cdot \mathbf{M}_{ij}^{(\text{SKNO})} \cdot (\chi^{(\text{SKNO})})_j^T \quad (51)$$

$$(\Delta \hat{\mathbf{A}})_{ij} = \text{conj}(\hat{V}_{L-1})_{ij} \cdot \hat{\mathbf{r}}_i^{(\text{SKNO})} \cdot \mathbf{M}_{ij}^{(\text{SKNO})} \cdot (\tilde{\chi}^{(\text{SKNO})})_j^T \quad (52)$$

$$\text{Grad}(\hat{V}_{L-1}^{(\text{SKNO})})_{ij} = \hat{\mathbf{A}}_{ij} \cdot \hat{\mathbf{r}}_i^{(\text{SKNO})} \cdot \mathbf{M}_{ij}^{(\text{SKNO})} \cdot (\tilde{\chi}^{(\text{SKNO})})_j^T, \quad (53)$$

where the weight $\Delta \chi \in \mathbb{R}^{N_p}$, complex tensors $\Delta \hat{\mathbf{B}} \in \mathbb{C}^{N_x \times N_p \times N_p}$ or $\mathbb{C}^{N_x \times N_p}$ and $\Delta \hat{\mathbf{A}} \in \mathbb{C}^{N_x \times N_p \times N_p}$ or $\mathbb{C}^{N_x \times N_p}$ are the changing values of parameters. $\text{conj}(\cdot)$ denotes element-wise taking the conjugate value of the input. $\mathbf{M}_{ij}^{(\text{SKNO})} = 1[(V_L^{(\text{SKNO})})_{ij} > 0]$ where $V_L^{(\text{SKNO})} = \text{ReLU}(V_L^{(\text{SKNO})})$.

Proof. Easy to derive these updating values by taking partial derivatives with respect to the parameters in propagators $\hat{\mathbf{B}}$ and $\hat{\mathbf{A}}$ and in the recovering operator χ . A notable point here is the conjugate gradient backpropagation path to the Fourier domain like the $\hat{\mathbf{r}}_i^{(\text{SKNO})}$ like in Equ.47.

The adjoint backward residual propagation and conjugate parameter updates shown above are directly derived from SKNO's spectral implementation. From Theorem "D.4, we can generalize the backward propagation framework for $d + 1$ -dimensional neural operators as follows

$$\Delta v_L(x, p) = \mathcal{Q}^*[r](x, p) = \chi^T(p)r(x) \quad (54)$$

$$\mathcal{K}^*[\Delta v](x, p) = \mathcal{K}[\Delta v](x, p) = \iint_{D_x \times D_p} \kappa(x, y, p, p') \Delta v(y, p') dy dp' \quad (55)$$

$$\Delta a(x) = \mathcal{P}^*[\Delta v_0](x) = \int_{D_p} \omega(p) \Delta v_0(x, p) dp, \quad (56)$$

where $r(x) := \Delta u(x) = u(x) - \mathcal{G}[a](x)$ denotes the residual between the solution $u(x)$ and the corresponding forward prediction $\mathcal{G}[a](x)$, and we define the adjoint operator of the lifting \mathcal{P}^* to have a p -integral form as the recovering operator \mathcal{Q} in Eq. 9, and vice versa. See Lemma D.5.

For previous d dimensional kernel integration designs, an additional matrix inversion is required when formulating the backpropagation process, whereas $d + 1$ dimensional neural operators are allowed to share the same kernel for the forward and adjoint operators, i.e., $\mathcal{K} = \mathcal{K}^*$. When $d + 1$ dimensional neural operators converge, the backpropagation updates (Rumelhart et al., 1986) stabilize within a PDE-specific equivalence class of parameters, up to a certain error tolerance.

Lemma D.5 (Adjoint of the recovering operator \mathcal{Q}). *Let $H_x := L^2(D_x)$ and $H_{x,p} := L^2(D_x \times D_p)$ with the standard L^2 inner products. Then \mathcal{Q}^* is the adjoint of \mathcal{Q} , i.e.*

$$\langle \mathcal{Q}[v], r \rangle_{H_x} = \langle v, \mathcal{Q}^*[r] \rangle_{H_{x,p}} \quad \forall v \in H_{x,p}, r \in H_x.$$

Proof. By definition of the L^2 inner product on H_x ,

$$\begin{aligned} \langle \mathcal{Q}[v], r \rangle_{H_x} &= \int_{D_x} (\mathcal{Q}[v])(x) r(x) dx \\ &= \int_{D_x} \left(\int_{D_p} \chi(p) v(x, p) dp \right) r(x) dx \\ &= \int_{D_x} \int_{D_p} v(x, p) \chi(p) r(x) dp dx. \end{aligned} \quad (57)$$

By definition of the L^2 inner product on $H_{x,p}$,

$$\begin{aligned} \langle v, \mathcal{Q}^*[r] \rangle_{H_{x,p}} &= \int_{D_x} \int_{D_p} v(x, p) (\mathcal{Q}^*[r])(x, p) dp dx \\ &= \int_{D_x} \int_{D_p} v(x, p) \chi(p) r(x) dp dx. \end{aligned} \quad (58)$$

Thus $\langle \mathcal{Q}[v], r \rangle_{H_x} = \langle v, \mathcal{Q}^*[r] \rangle_{H_{x,p}}$ for all v, r , so \mathcal{Q}^* is the adjoint of \mathcal{Q} . Similar proof for the adjoint between \mathcal{P} and \mathcal{P}^* .

Entanglement Moreover, we novelly compute the entanglement entropy values after each $d + 1$ dimensional propagation, inspired by the quantum view in Remark D.6, and plot some randomly selected cases of them in Fig.7: Compared to FNO, SKNO introduces stronger perturbations on the singular spectrum after $\mathcal{L}_l[v_l]$, cooperated with effectively controlling the sparsity of the energy distribution by σ_l . In addition, the PDE-aligned design in the $\mathcal{L}_l[v_l]$ of SKNO makes it more flexible to reduce entanglement in the final linear stage further, while FNO is purely driven by the squared-loss objective to substantially perturb the $(d + 1)$ -dimensional signal without an implicit structural regularization along p , which leads to increased entanglement entropy in some cases.

Remark D.6 (Propagation of the $d + 1$ Entangled States). From (Jin et al., 2022), if \mathcal{P} is chosen as a linear layer, $v_0(x, p)$ is a pure global quantum state without entanglement between the original x and p spaces. In neural operators, the initial quantum state V_0 becomes entangled during the (non-linear) forward propagation. A measure of the degree of such entanglement between two subsystems of a composite quantum system is the entanglement entropy, which can be calculated numerically using Algorithm 1.

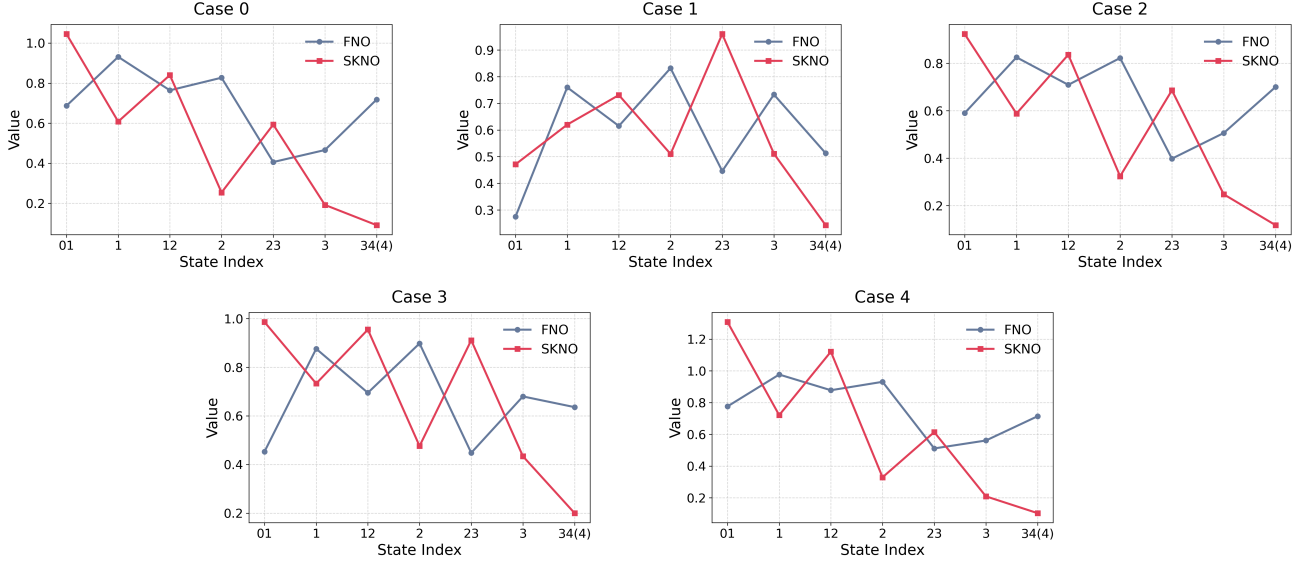


Figure 7. Entanglement entropy of intermediate layer outputs. For five randomly selected test cases from the test set, the final entanglement entropy of SKNO is consistently lower than that of FNO, indicating that the $(d + 1)$ -dimensional design of SKNO yields representations that are less entangled and exhibit a more energy-concentrated distribution. On the horizontal axis, a two-digit index (e.g., "01") denotes the output after the \mathcal{L}_0 and before the σ_0 between v_0 and v_1 , whereas a single-digit index (e.g., "1") denotes v_1 as the output of the first propagator ($\sigma_0 \circ \mathcal{L}_0$). Note that the initial index "0" corresponds to v_0 . Under a purely linear lifting operator without positional encoding, v_0 is typically separable, so all curves effectively start from an unentangled state at the origin and evolve through the forward propagation.

E. Visualization

Patterns with different scales We visualize cases to highlight the patterns with different scales of our SKNO. These subplots are plotted over all p values after the $d + 1$ dimensional evolution. Cases include the 1D Burgers, 2D Darcy Flow, and 2D incompressible Navier-Stokes benchmarks, shown in Fig. ??, Fig. 8 and Fig. 11 respectively.

Algorithm 1 Entanglement Entropy Numerical Calculation

Require: V_l , $l = 0, 1, \dots, L$.

Ensure: Entanglement Entropy S_l .

Perform singular value decomposition:

$$V_l = \Psi_l \Lambda_l (\Phi_l)^T$$

where $\Sigma_l = \text{diag}((\lambda_1)_l, (\lambda_2)_l, \dots, (\lambda_{N_p})_l)$.

Normalize Schmidt coefficients:

$$(c_m)_l \leftarrow \frac{(\lambda_m)_l}{\sqrt{\sum_{m'} (\lambda_{m'})_l^2}}.$$

Compute entanglement entropy:

$$S_l \leftarrow - \sum_m (c_m)_l^2 \log((c_m)_l^2).$$

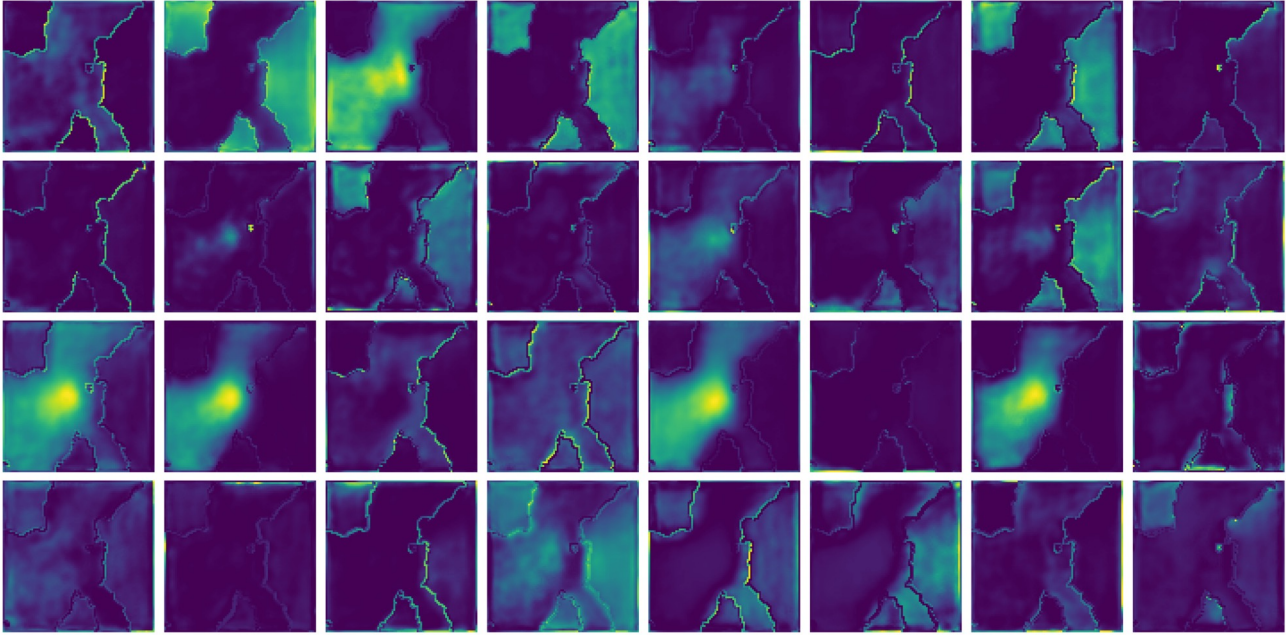


Figure 8. Pattern visualization of the 2D Darcy case. According to the discontinuities in the inputs, SKNO learns patterns at different scales.

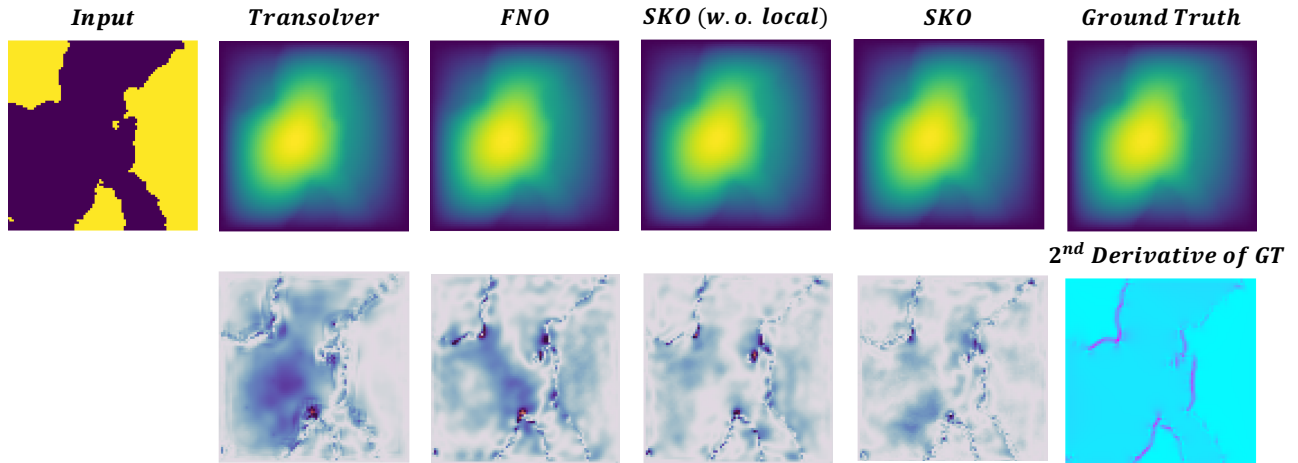


Figure 9. Prediction, error, and second derivative of ground truth visualization for 2D Darcy. The top row shows predictions from different models and ground truth, while the bottom row presents the corresponding error visualizations and the second derivative of the ground truth.

Table 6. Table of key notations.

Notation	Meaning
Problem Setup	
$D_x \subset \mathbb{R}^d$	Original domain where functions are defined with d dimensions
$x \in D_x$	Query position of in/output functions in the d dimensional domain
$a(x) \in \mathcal{A}$	Input function
d_a	The length of concatenated input vectors
$u(x) \in \mathcal{U}$	Output function
d_u	The length of concatenated output vectors
$\mathcal{G}[\cdot]$	Solution operator
$d + 1$ dimensional NO Framework	
p	The auxiliary dimension variable composing $d + 1$ dimensional PDEs
D_p	Domain where the auxiliary variable p lives
$v(x, p)$	Transformed function in the $d + 1$ dimensional domain $D_x \times D_p$
$\mathcal{P}[\cdot]$	Operator lifts input signals into ones with grids in $D_x \times D_p$
$\mathcal{L}[\cdot]/\mathcal{L}_l[\cdot]$	The (l -th) learnable linear block capturing $d + 1$ dimensional operators
$\sigma_l(\cdot)$	The (l -th) element-wise activation function or 2-layer MLP
$\mathcal{Q}[\cdot]$	Operator recovers evolved $d + 1$ dimensional signals into outputs
Others	
$\widehat{(\cdot)}$	The original function/signal represented in Fourier domain of x
$\widetilde{(\cdot)}$	The original function/signal represented in Fourier domain of p
$\widehat{(\cdot)}$	The original operator/matrix represented in Fourier domain of x
$\widetilde{(\cdot)}$	The original operator/matrix represented in Fourier domain of p
N_x	The number of grid indices on D_x
N_p	The number of grid indices on D_p
k_x	The number of grid indices on the transformed domain after aggregation on D_x
k_p	The number of grid indices on the transformed domain after aggregation on D_x

Table 7. Complete best training configurations

Model	Epochs	Batch Size	# Modes <i>OR</i> Slices	# Layers	# Pos. Feat. / Type	# Sub-grid \times size on D_p
1D Heat (Linear Block)						
Transolver	500	20	4	1	N.A.	1×4
FNO	500	20	1	1	N.A.	1×4
SKNO	500	20	1	1	N.A.	1×4
1D Advection (Linear Block)						
Transolver	500	4	8	1	N.A.	1×16
FNO	500	20	8	1	N.A.	1×16
SKNO	500	20	8	1	N.A.	1×16
1D Burgers						
Transolver	500	4	64	8	64 / Ref.	8×32
FNO	500	20	16	4	1 / Abs.	1×64
SKNO	500	20	16	4	1 / Abs.	1×64
2D Gray-Scott						
Transolver	500	2	32	8	$8^2 = 64$ / Ref.	8×32
FNO	500	10	12	4	2 / Abs.	1×24
SKNO	500	10	12	4	2 / Abs.	1×24
2D Shallow-Water						
Transolver	100	2	32	8	$8^2 = 64$ / Ref.	8×32
FNO	100	20	8	4	2 / Abs.	1×24
SKNO	100	20	8	4	2 / Abs.	1×24
2D Darcy Flow						
Transolver	500	4	64	8	$8^2 = 64$ / Ref.	8×16
FNO	500	20	12	4	2 / Abs.	1×32
SKNO	500	20	12	4+1	2 / Abs.	1×32
2D Incompressible Navier-Stokes						
Transolver	500	2	32	8	$8^2 = 64$ / Ref.	8×32
FNO	8000	20	12	4	2 / Abs.	1×24
SKNO	3000	20	12	4+1	2 / Abs.	1×24
3D Compressible Navier-Stokes						
Transolver	100	2	32	8	$8^3 = 512$ / Ref.	8×32
FNO	100	10	16	4	3 / Abs.	1×32
SKNO	100	10	16	4	3 / Abs.	1×32
3D Rayleigh-Taylor Instability						
Transolver	250	2	32	8	$8^3 = 512$ / Ref.	8×32
FNO	250	10	16	4	3 / Abs.	1×32
SKNO	250	10	16	4+1	3 / Abs.	1×32
ERA5 Wind Field Prediction						
Transolver	50	2	64	4	$8^2 = 64$ / Ref.	8×8
FNO	50	2	10	4	2 / Abs.	1×20
SKNO	50	2	10	4	2 / Abs.	1×20

Table 11. Results on 2D Darcy under several alternative implementations in both the d dimensional and $d + 1$ dimensional frameworks. The two rightmost $d + 1$ dimensional neural operator implementations outperform all d dimensional baselines (Lu et al., 2021; Li et al., 2021; Hao et al., 2023; Li et al., 2023b; Wu et al., 2023; Raonic et al., 2023a; Wu et al., 2024a) on the left. *2Stack-FNO*: simply stacks two Fourier layers in the d dimensional setting, thereby ignoring operator design along p . *SKNO-Attention*: replaces the spectral operator in SKNO with the attention-based aggregation module from (Wu et al., 2024a).

Model	DeepONet	GNOT	OFormer	LSM	CNO	FNO	2Stack-FNO	Transolver	SKNO-Attention	SKNO (Ours)
Rel. L_2 Err.	0.0609	0.0102	0.0121	0.0065	0.0060	0.0062	0.0061	0.0058	0.0058	0.0055
Training Time	5.20 min	22.58 min	21.91 min	20.37 min	63.34 min	10.21 min	13.35 min	115.48 min	76.90 min	17.59 min

1D Burgers Equation								
Grid Size	128	256	512	1024	2048	4096	8192	Variance
Transolver	6.277E-03	7.186E-03	8.058E-03	8.546E-03	8.800E-03	8.928E-03	8.993E-03	9.04472E-07
FNO	6.479E-04	6.476E-04	6.480E-04	6.477E-04	6.454E-04	6.455E-04	6.455E-04	1.33912E-12
SKNO	5.475E-04	5.489E-04	5.490E-04	5.489E-04	5.488E-04	5.487E-04	5.487E-04	2.53997E-13
2D Darcy Flow								
Grid Size	$(22)^2$	$(29)^2$	$(43)^2$	$(85)^2$	$(141)^2$	$(211)^2$	$(421)^2$	Variance
FNO	9.813E-02	7.718E-02	4.956E-02	6.165E-03	3.044E-02	3.897E-02	4.939E-02	7.83082E-04
SKNO	7.739E-02	6.302E-02	4.122E-02	5.551E-03	2.366E-02	3.271E-02	4.112E-02	4.90633E-04

Table 12. Prediction errors of neural operators on the 1D Burgers equation and 2D Darcy flow across different grid sizes. The table also reports the variance of errors over grid resolutions, highlighting SKNO’s superior accuracy and stability.

Table 13. Performance of neural operator models on 2D Shallow Water and 3D Compressible NS benchmarks. On the 2D Shallow Water, we train models on a randomly selected resolution and evaluate them at the highest resolution. -: No 3D implementation available; *: Requires predefining the resolution, here trained on the highest resolution; **: For fairness, training times are all reported on the highest resolutions. The CNO model is described in ((Raonic et al., 2023a)).

Models	DeepONet	CNO	FNO	Transolver	SKNO
2D Shallow Water					
Rel. L_2 Err.	0.0902*	0.0085*	0.0030	0.0088	0.0027
Training Time**	8.59 min	49.26 min	11.43 min	128.64 min	20.85 min
3D Compressible Navier-Stokes					
Rel. L_2 Err.	0.5628	-	0.2631	0.2947	0.2376
Training Time	3.90 min	-	10.12 min	361.41 min	23.33 min

Wind U						
Grid Size	$(32)^2$	$(64)^2$	$(128)^2$	$(256)^2$	$(512)^2$	Variance
FNO	6.272E-02	6.525E-02	6.872E-02	7.097E-02	7.212E-02	1.23506E-05
SKNO	6.164E-02	6.237E-02	6.366E-02	6.445E-02	6.495E-02	1.54763E-06
Wind V						
Grid Size	$(32)^2$	$(64)^2$	$(128)^2$	$(256)^2$	$(512)^2$	Variance
FNO	2.165E-01	2.326E-01	2.430E-01	2.476E-01	2.498E-01	1.49635E-04
SKNO	1.969E-01	2.027E-01	2.108E-01	2.156E-01	2.181E-01	6.30471E-05

Table 14. Zero-shot super-resolution evaluation on ERA5 wind field prediction. As the grid resolution increases, SKNO exhibits substantially lower growth in relative L_2 error compared to FNO, leading to a pronounced accuracy advantage on the finest grid $(512)^2$.

Table 15. Results for ERA5 wind field prediction.

Model	Performance	Training Time	Wind U Error	Wind V Error
	FNO		0.76 min	7.064e-2
Transolver		10.81 min	6.291e-2	2.007e-1
SKNO		1.75 min	6.11e-2	1.920e-1

Table 16. Comparison of different configurations with zero, one, and two local propagators. Results show that adding local aggregation layers helps signals integrate residual information more effectively with a lower level of entanglement.

Metric	w.o. Local Prop	1 Local Prop	2 Local Props
Rel. L_2 Err.	5.717	5.555	5.289
Entanglement Entropy (Before Recovering)	2.286	1.849	1.277

Table 17. Performance of models on 2D stress and 2D strain benchmarks (Rashid et al., 2022; Burark et al., 2024). The reported average (Avg.) training time is the mean over these two benchmarks, with all other configurations identical except for the type of predicted field.

Models	DeepONet	FNO	Transolver	SKNO
<i>2D Stress</i>				
Rel. L_2 Err.	0.3891	0.0622	0.0481	0.0472
<i>2D Strain</i>				
Rel. L_2 Err.	0.5439	0.0575	0.0465	0.0463
Avg. Training Time	4.15 min	9.43 min	117.39 min	19.36 min

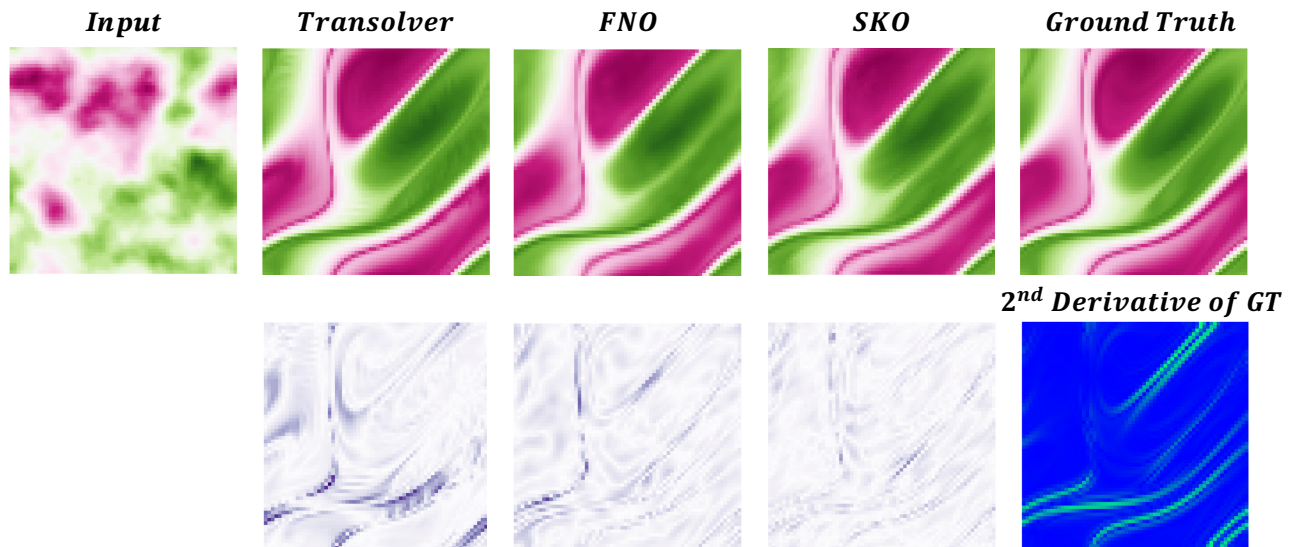


Figure 10. Prediction, error, and second derivative of ground truth (GT) visualization for 2D Darcy.

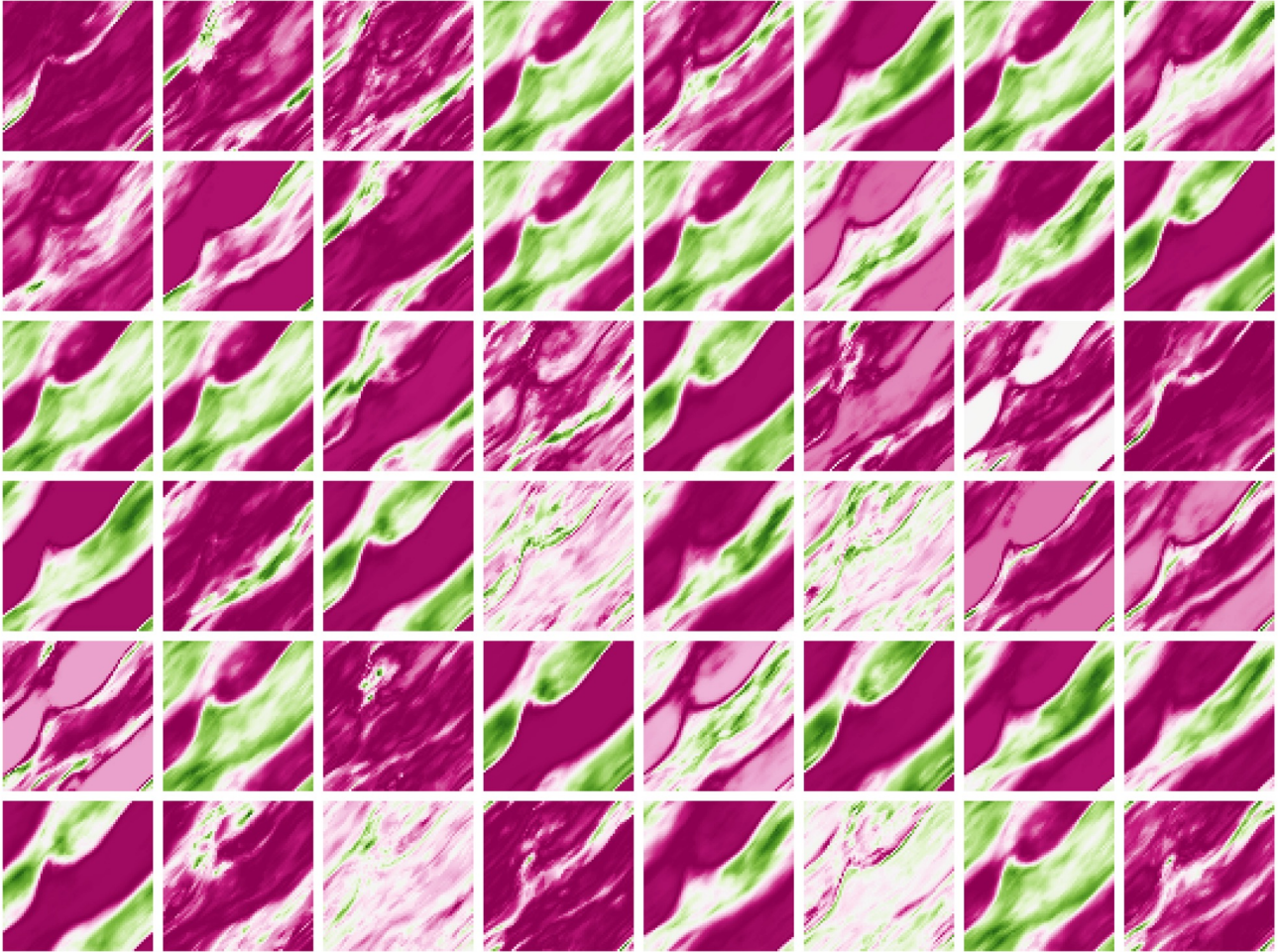


Figure 11. Pattern visualization of the 2D Navier-Stokes case.

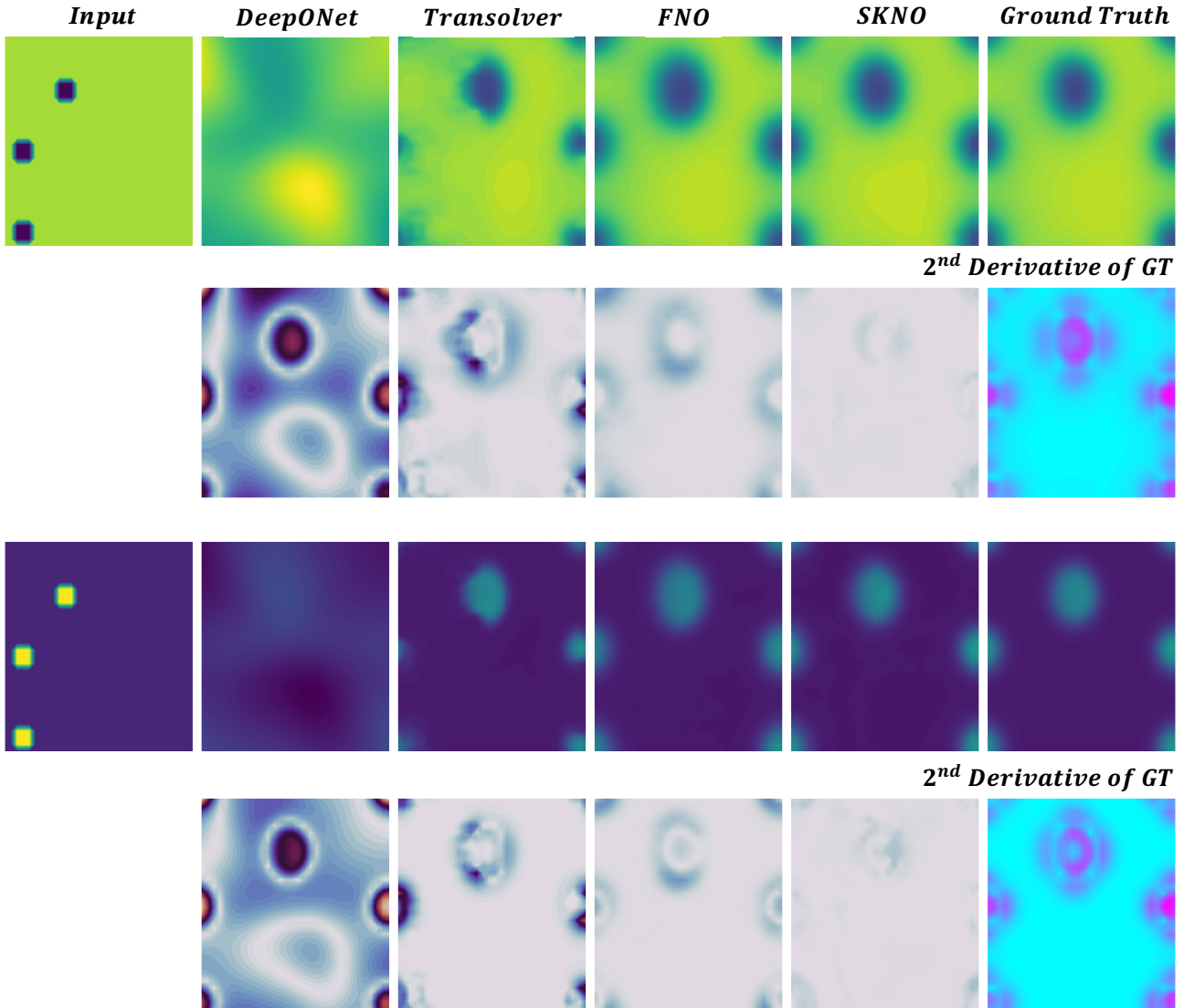


Figure 12. Visualization of the 2D Gray-Scott case. Top: u ; Bottom: v . SKNO achieves the lowest error on both.

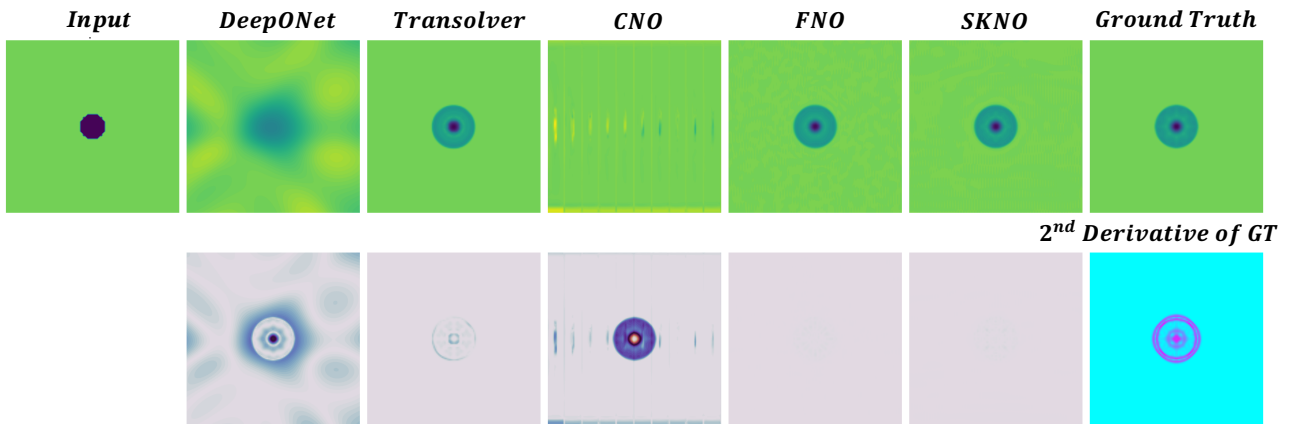


Figure 13. Visualization of the 2D Shallow-Water case with randomly mixed training data at different resolutions, evaluated at the highest resolution.

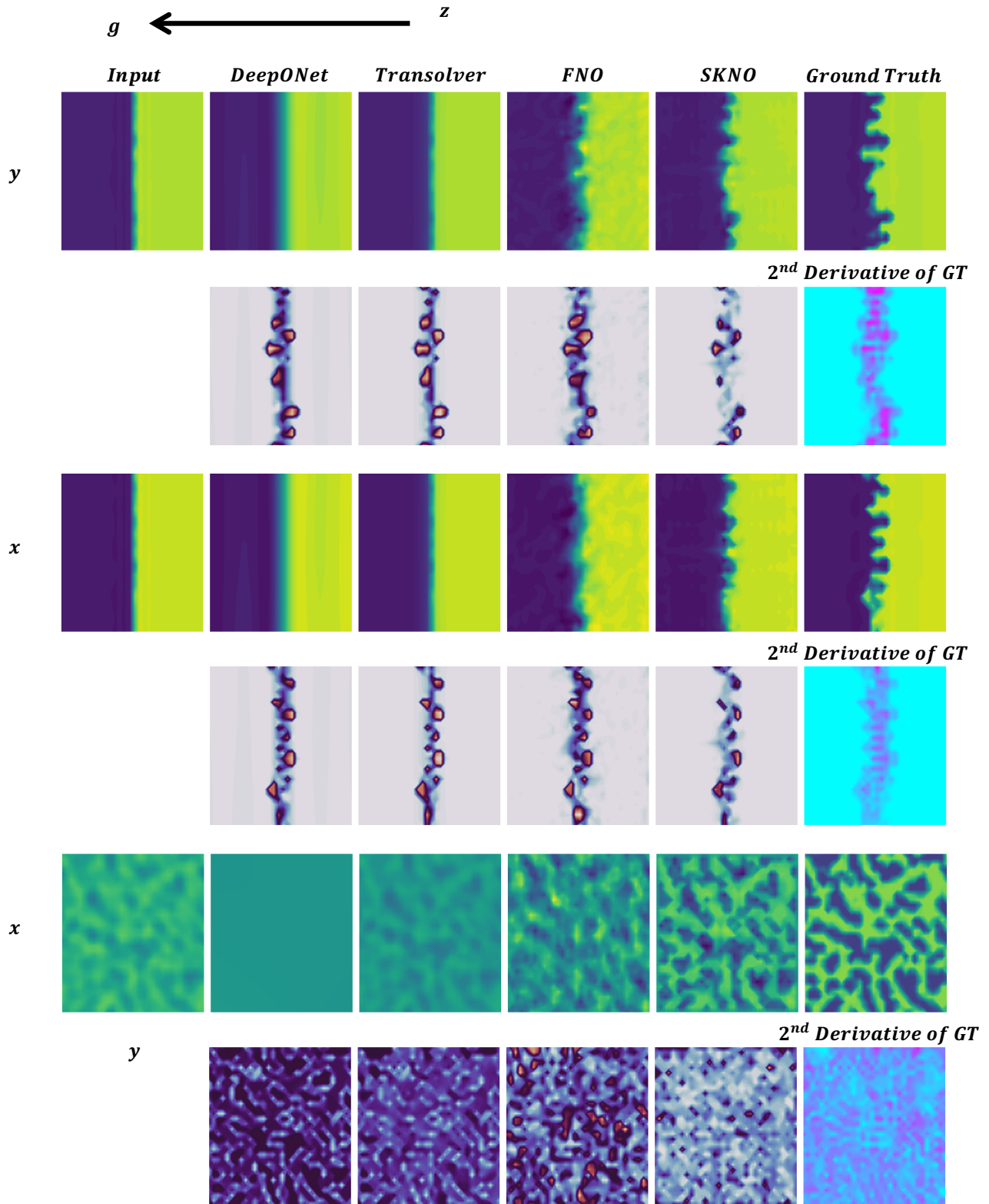


Figure 14. Visualization of the 3D Rayleigh–Taylor instability case. All slices are parallel to the coordinate planes, and their intersection points are chosen as the grid points nearest to the center of the box. We show a representative extreme case, namely predicting the output field after 20 steps from a perturbed initial condition. While other lightweight methods largely fail, SKNO can still capture the overall flow trends and the interfacial surfaces between the fluids with different densities. g represents the gravity direction.

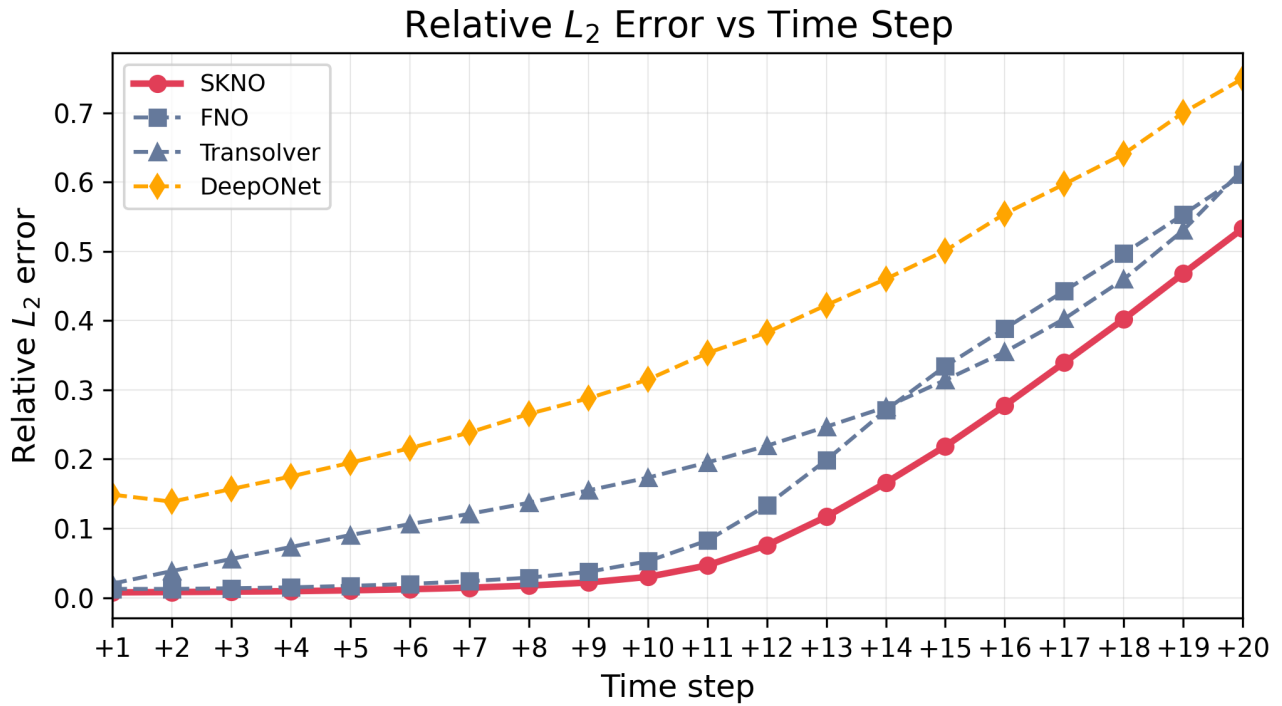
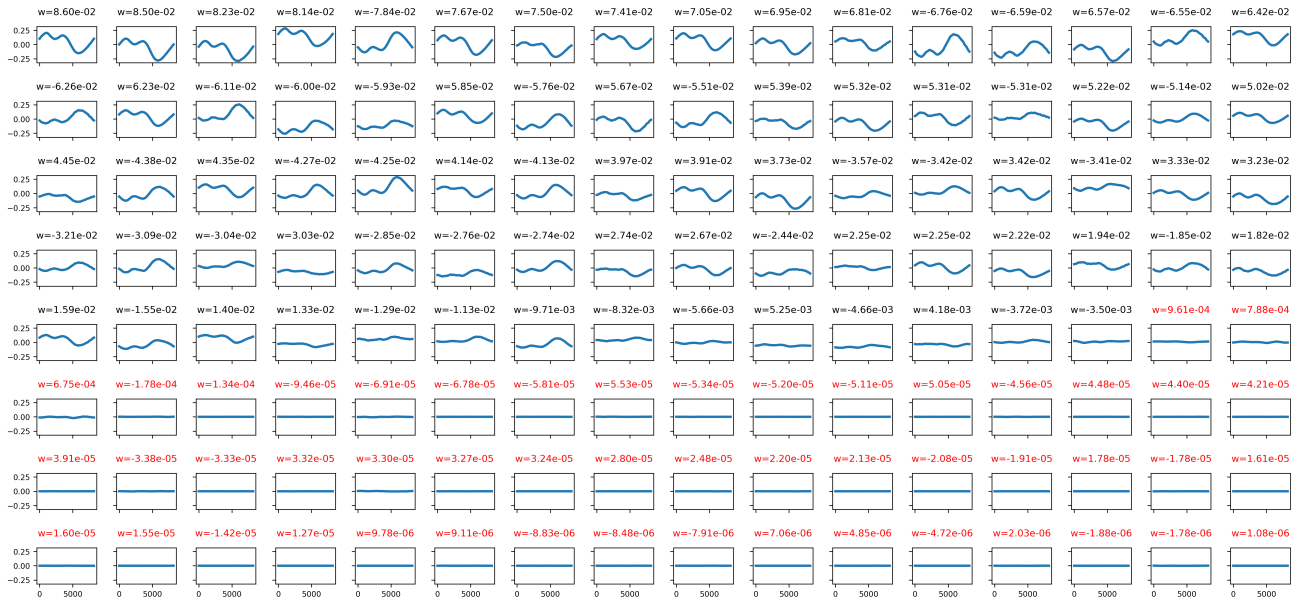


Figure 15. Visualization of zero-shot predictions at future time steps. For the 2D incompressible Navier–Stokes with viscosity 1×10^{-4} (Li et al., 2021), all models are autoregressively evaluated over the twenty time steps following the input time. SKNO maintains its state-of-the-art performance on both the seen temporal range (+1 to +10) and the unseen temporal range (+11 to +20), achieving a substantial performance margin over competing methods. Compared with FNO, Transolver, and DeepONet, SKNO achieves average error reductions of 34.5%, 58.7%, and 74.5%, respectively, across all shown predictions. Note that even on the first predicted step, SKNO attains an error of 0.0076, outperforming FNO (0.0127), Transolver (0.0202), and DeepONet (0.1488).

All 128 Output Pattern fields in the Dictionary (Sorted by the absolute value of weights)

FNO



SKNO

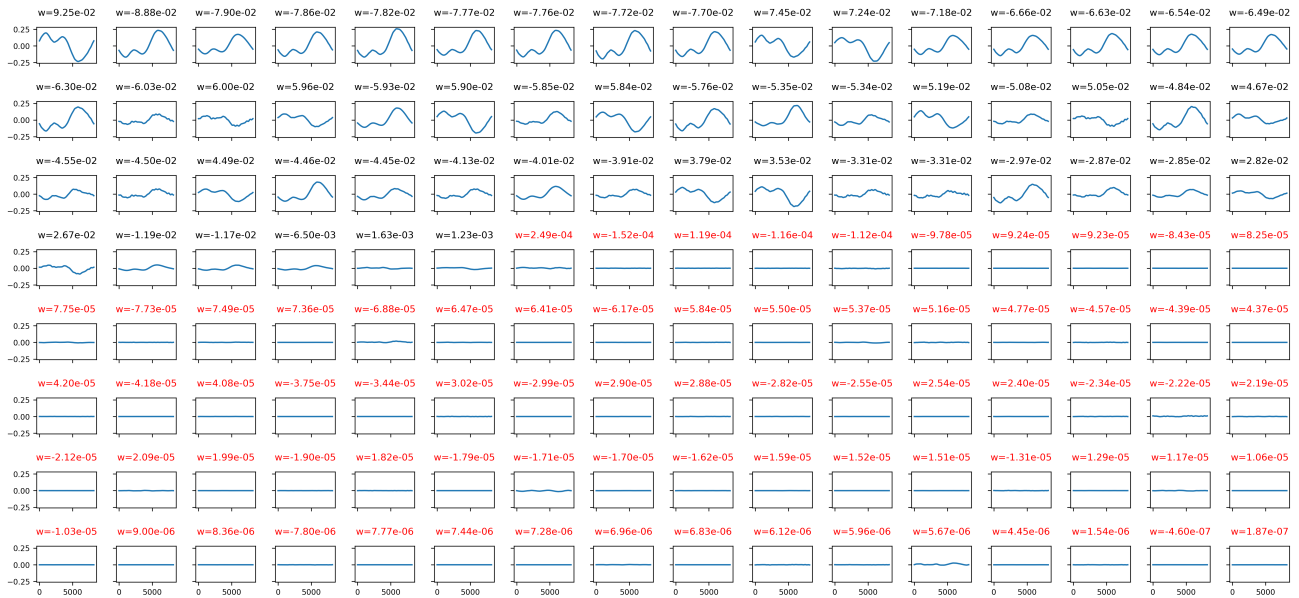


Figure 16. Visualization of paired output weights and pattern fields. All pattern fields are sorted in descending order of the absolute value of their associated output weights, and values marked in red lie below the contribution threshold of 10^{-3} . Even with the same sufficiently large N_p , the relative L_2 error of SKNO on the testing data $6.546e - 4$ is still larger than FNO $6.603e - 4$.